Comprehensive Analysis and Review of Techniques for Precise Evaluation of Aerodynamic Derivatives

Ahmed M. Eid [*], Ashraf M. Kamal [†], Mohamed Y. Zakaria [‡], and Omar F. Abdel-Hameed [§]
Military Technical Collage, Cairo, Egypt

This paper presents a comprehensive review of the techniques used to evaluate aerodynamic derivatives. The review covers analytical, empirical, semi-empirical, numerical, and experimental methods for determining aerodynamic derivatives. The pros and cons of every approache are discussed and highlighted. The paper also provides a deep overview of the dynamic test methodologies used to characterize flight behavior in models. The review concludes that while experimental methods remain the most effective and precise technique for obtaining aeromechanical derivatives, modern numerical approaches have significantly enhanced the accuracy of these methods with respect to more than one point of view, such as cost. This paper is a valuable resource for researchers, engineers, and aviation enthusiasts seeking to gain a deeper understanding of aerodynamic derivatives and their applications. The comprehensive coverage and valuable insights presented in this review make it a valuable addition to the literature on aerodynamics.

I. Nomenclature

Symbols

a_∞ = Sound speed
C_{lp} = Derivative of the rolling moment coefficient with respect to the roll rate
C_{lq} = Derivative of the rolling moment coefficient with respect to the pitch rate
C_{lr} = Derivative of the rolling moment coefficient with respect to the yaw rate
$C_{l\dot{\beta}}$ = Derivative of the rolling moment coefficient with respect to the angle of sideslip rate
$C_{l\dot{\alpha}}$ = Derivative of the rolling moment coefficient with respect to the angle of attack rate
C_{mp} = Derivative of the pitching moment coefficient with respect to the roll rate
C_{mq} = Derivative of the pitching moment coefficient with respect to the pitch rate
C_{mr} = Derivative of the pitching moment coefficient with respect to the yaw rate
$C_{m\dot{\alpha}}$ = Derivative of the pitching moment coefficient with respect to the angle of attack rate
$C_{m\alpha}$ = Derivative of the pitching moment coefficient with respect to the angle of attack
$C_{m\dot{\beta}}$ = Derivative of the pitching moment coefficient with respect to the angle of sideslip rate
C_{np} = Derivative of the yawing moment coefficient with respect to the roll rate
C_{nq} = Derivative of the yawing moment coefficient with respect to the pitch rate
C_{nr} = Derivative of the yawing moment coefficient with respect to the yaw rate
$C_{n\dot{\alpha}}$ = Derivative of the yawing moment coefficient with respect to the angle of attack rate
$C_{n\dot{\beta}}$ = Derivative of the yawing moment coefficient with respect to the angle of sideslip rate
C_i = Aerodynamic force or moment coefficients, $i = L, D, m, l, n$
C_l = Rolling moment coeff.
C_m = Pitching moment coeff.
C_n = Yawing moment coeff.
C_p = Pressure coeff.
D = Coefficient matrix
f = Circular frequency of oscillatory

---

[*] MSc. Student, Aircraft Mechanics Department, Military Technical Collage.

[†] Assistant Professor, Aircraft Mechanics Department, Military Technical Collage

[‡] Associate Professor, Aircraft Mechanics Head of Department, Military Technical Collage

[§] Professor, Aircraft Mechanics Department, Military Technical Collage

I_z = Moment of inertia to z axis
k = Apparatus damping coeff.
N_H = Number of harmonics
N_T = Number of sample points
n_z = Damping coefficient
p = Roll rate
q = Pitch rate
Q = Conservative variable
$\bar{q}$ = Non dimensional pitch rate
r = Yaw rate
R = Flux vector
α = Angle of attack
$\dot{\alpha}$ = Angle of attack rate
$\bar{\dot{\alpha}}$ = Non dimensional angle of attack rate
β = Angle of sideslip
$\dot{\beta}$ = Angle of sideslip rate
γ = Specific heat ratio
$\Delta\alpha$ = Additional angle of attack
ε = Angle between the body and wind axis
ϵ = Phase shaft angle
θ = Pitch angle
$\dot{\theta}$ = Pitch angle rate, equal to q
ρ = Density
σ = Apparatus stiffness coefficient
φ = Angle of roll
ψ = Angle of yaw
$\bar{\omega}$ = Frequency parameter

Abbreviations

AGARD = Advisory Group for Aerospace Research and Development
CFD = Computational Fluid Dynamics
DATCOM = Data Compendium
DLR = Deutsches Zentrum für Luft- und Raumfahrt
DNW = German–Dutch wind tunnel
NACA = National Advisory Committee for Aeronautics
NASA = National Aeronautics and Space Administration
NS = Navier Stokes
SACCON = Stability and Control Configuration
SDM = Standard Dynamic Model
TCR = Transcruiser configuration

II. Introduction

A dynamic experiment conducted in a wind tunnel is the most effective method for acquiring model-scale dynamic stability parameters at certain Reynolds and Mach no. values. Essentially, this knowledge may also be acquired by model testing on different sorts of systems [1]. Examples of such testing include studies conducted in the fields of aeroballistics or hypervelocity regimes, as well as outdoor free-flight tests via radio-controlled models. Additionally, spin tunnel experiments are carried out as well. Nevertheless, all of these strategies share comparable limitations. During trials conducted at high Reynolds numbers. In addition, a few of them may be utilized to derive the dynamic stability derivatives from the operational history of the model, but this practice is hardly employed. Consequently, these approaches are mostly used to visually analyze the stability characteristics and maneuvers of aircraft, especially at low Reynolds numbers. Large-scale flying experiments can also yield dynamic stability derivatives. Although the availability of test findings may have a substantial influence on the design time of new airplanes, the values of several dynamic stability parameters can't be associated till the full-scale flight test is conducted. The flight behavior of an existing aircraft has correlations that are especially valuable for studying high angle-of-attack stall characteristics. These correlations help us comprehend the relative significance of different derivatives and give an accurate evaluation of the already employed techniques of motion analysis. In recent times, stability derivatives are fixed values that indicate the rate at which a certain aerodynamic coefficient changes with a variable that might potentially be zero. In view of the current interest in aviation, where certain displacement variables such as alpha, beta, and spin rate have particularly high values, we examine the stability derivatives being a function of these variables then utilize the appropriate local value. Require completion. For any equilibrium function.

A stability derivative is a measure of how a small change in the steady state flight condition affects the various attitude parameters and their rates of change over time. It is derived from the standard form of equations of motion, where the result of a small perturbation is determined by a linear combination of these contributions. The traditional stability derivatives are fixed values that quantify the rate of change of a certain aerodynamic coefficient at a particular position when the corresponding variable is equal to zero. In light of the present focus on flight tests conducted at elevated levels of certain displacement factors (such as α, β, and spin rate), it is necessary to analyze stability derivatives as variables dependent on these factors and to utilize the appropriate local values for each state of equilibrium. When the changes reflected by these functions occur rapidly or when the disturbances are no longer insignificant, it may be necessary to replace a constant derivative with an analytical expression that describes its fluctuation near the equilibrium point. It is important to recognize that a stability derivative is not always a constant, but can sometimes depend on one or more displacement factors. The experimental approaches for acquiring the requisite knowledge have remained mostly unaltered from previous times. Rather to determining a singular value, it is possible to gather a sufficient amount of data points to characterize a function, hence significantly augmenting the number of required tests. Therefore, it is now imperative to carry out these tests with greater efficiency than before. A larger number of additional derivatives may demand a significant rise in the quantity of tests that are necessary. Historically, the range of interest in dynamic derivatives was often limited to the three damping derivatives, sometimes mentioning the dynamic cross derivatives. However, a modern fighter design may need up to three times the number of variations. Tables can also be created for the dynamic force derivatives, although these are usually less important and will not be extensively covered here. Dynamic force derivatives can be particularly relevant in some situations, such as when assessing direct side force or direct-lift controls, or when transferring dynamic moment derivatives across different axes.

III. Analytical Techniques

In the evolving landscape of aerodynamics, the journey from the initial development of analytical procedures to sophisticated numerical simulations marks a significant chapter in scientific inquiry. This narrative unfolds with contributions from several key figures, each bringing forward innovations that have propelled the field into new frontiers. Bryan [2] laid the groundwork with the construction of a mathematical model, pioneering the use of numerical simulations to explore dynamic derivatives. His work addressed the early challenges encountered due to the limited understanding and application of numerical approaches, which were initially confined to relatively simple configurations and subject to various simplifications. Building on this foundational work, Theodorsen [3] introduced a groundbreaking approach for the calculation of unsteady aerodynamics, specifically targeting the NACA 0012 airfoil in harmonic oscillation. Through his theory, predicated on potential flow, he facilitated the computation of both acceleration and rotatory derivatives, significantly advancing the field's capability to model aerodynamic behaviors. Further refinement in the analytical methodologies came with advancements in Finding the directional and lateral derivatives for supersonic flow over thin airfoils [4]. These improvements expanded the applicability of mathematical models to more complex flight conditions, enhancing the precision of aerodynamic analyses. A pivotal contribution to this narrative was made by Bernard Etkin [5], whose rigorous and concise analytical techniques for calculating static and control derivatives of airplanes set new standards in the field. Etkin's methodologies, deeply rooted in analytical precision, provided a comprehensive framework for estimating crucial aerodynamic parameters for example lift, drag, pitching moment, and control effectiveness coefficients. Inspired by Etkin's significant contributions, a proposed methodology emerged that leverages his analytical frameworks and equations to offer a systematic means for deriving key parameters. This approach not only underscores the precision and effectiveness of Etkin's techniques but also offers researchers, engineers, and designers a robust tool for assessing aircraft performance, stability, and control characteristics. The integration of

Etkin's analytical techniques into this methodology ensures accurate calculations, contributing to a deeper understanding of aircraft behavior and supporting informed decision-making in aircraft design and optimization. The formulas that are frequently used are collected in Tables 1 and 2. While the principle behind the analytical method is straightforward, its application to complex scenarios has proven exceedingly challenging, prompting a shift toward more sophisticated alternatives.

Table 1 Represents the longitudinal derivatives based on the analytical methods derived by Etkins

	$\boldsymbol{C}_{\mathbf{x}}$	$\boldsymbol{C}_{\mathbf{z}}$	$\boldsymbol{C}_{\mathbf{m}}$
$\hat{\boldsymbol{u}}\dagger$	$\mathrm{M}_0\left(\frac{\partial C_T}{\partial \mathrm{M}}-\frac{\partial C_D}{\partial \mathrm{M}}\right)-\rho u_0^2\frac{\partial C_D}{\partial p_d}+C_{T_u}\left(1-\frac{\partial C_D}{\partial C_T}\right)$	$-\mathrm{M}_0\frac{\partial C_L}{\partial \mathrm{M}}-\rho u_0^2\frac{\partial C_L}{\partial p_d}-C_{T_u}\frac{\partial C_L}{\partial C_T}$	$\mathrm{M}_0\frac{\partial C_m}{\partial \mathrm{M}}+\rho u_0^2\frac{\partial C_m}{\partial p_d}+C_{T_u}\frac{\partial C_m}{\partial C_T}$
$\boldsymbol{\alpha}$	$C_{l_0}-C_{D_\alpha}$	$-\left(C_{L_\alpha}+C_{D_0}\right)$	$-a\left(h_n-h\right)$
$\dot{\boldsymbol{\alpha}}$	Neg.	$*-2a_tV_H\frac{\partial\epsilon}{\partial\alpha}$	$*-2a_tV_H\frac{l_t}{\bar{c}}\frac{\partial\epsilon}{\partial\alpha}$
$\hat{\boldsymbol{q}}$	Neg.	$*-2a_tV_H$	$*-2a_tV_H\frac{l_t}{\bar{c}}$

Neg. means usually negligible.
* means contribution of the tail only, formula for wing-body not available.
$\dagger C_{T_u}=\frac{(\partial T/\partial u)_0}{\frac{1}{2}\rho u_0 S}-2C_{T_0};C_{T_0}=C_{D_0}+C_{w_0}\sin\theta_0$

Table 2 Represents the lateral derivatives based on the analytical methods derived by Etkins

	$\boldsymbol{C}_{\mathbf{y}}$	$\boldsymbol{C}_{\mathbf{l}}$	$\boldsymbol{C}_{\mathbf{n}}$
$\boldsymbol{\beta}$	$*-a_F\frac{S_F}{S}\left(1-\frac{\partial\sigma}{\partial\beta}\right)$	N.A.	$*a_FV_v\left(1-\frac{\partial\sigma}{\partial\beta}\right)$
$\hat{\boldsymbol{p}}$	$*-a_F\frac{S_F}{S}\left(2\frac{Z_F}{b}-\frac{\partial\sigma}{\partial\hat{p}}\right)$	N.A.	$*a_FV_V\left(2\frac{z_F}{b}-\frac{\partial\sigma}{\partial\hat{p}}\right)$
$\hat{\boldsymbol{r}}$	$*a_F\frac{S_F}{S}\left(2\frac{l_F}{b}+\frac{\partial\sigma}{\partial\hat{r}}\right)$	$*a_F\frac{S_F}{S}\frac{z_F}{b}\left(2\frac{l_F}{b}+\frac{\partial\sigma}{\partial\hat{r}}\right)$	$*-a_FV_V\left(2\frac{l_F}{b}+\frac{\partial\sigma}{\partial\hat{r}}\right)$

* Means contribution of the tail only, formula for wing-body not available; $V_F/V=1$.
N.A. means no formula available

IV. Empirical and Semi-empirical Methods

In the realm of aerodynamic analysis, where analytical methods may falter in the face of complexity and computational fluid dynamics (CFD) techniques are yet to be fully developed, empirical and semi-empirical engineering methodologies have emerged as viable alternatives. These methodologies serve as invaluable tools in scenarios where traditional analytical techniques are not feasible. Empirical methods entail the fitting of formulae or charts correlating dynamic derivatives with parameters gleaned from aircraft dynamic derivative data obtained through wind tunnel experiments or flight tests. Notably, the DATCOM program stands as a prominent example of this empirical approach [6]. Leveraging vast repositories of aerodynamic data, DATCOM aids in the conceptual and preliminary phases of aircraft design, facilitating essential aerodynamic evaluations. However, it is important to note that DATCOM-derived dynamic derivatives primarily rely on geometric considerations, thereby necessitating only a limited set of factors to assess stability [7]. For instance, reference [8] delves into the lateral dynamic derivatives of airplane such as F-15, extracted from DATCOM datasets spanning low and high speeds. Under normal operational conditions, DATCOM yields precise results. Yet, complexities arise when attempting to model typical layouts or nonlinear flow fields, posing challenges in obtaining reliable outcomes. To enhance the predicted qualities of empirical techniques, semi-empirical procedures have been developed. These approaches, grounded in a fusion of assumptions and experimental evidence, manifest as rudimentary mathematical models of physical phenomena. Noteworthy among these are Newtonian impact theory and piston theory-based methodologies, widely utilized to facilitate the calculation of dynamic derivatives. However, it is imperative to recognize that these procedures maintain reliability solely within predefined ranges, underscoring the need for caution in their application.

A. Newtonian Impact Theory Based Method

Newtonian impact theory, first formulated in 1726, is considered a fundamental concept in the study of aerodynamic drag [9]. This theory, grounded in the mechanics of individual gas particles during inelastic collisions, proposes that the pressure exerted on a body influences the momentum of particles along the surface direction. Illustrated through the example of a plate moving uniformly through air, the pressure coefficient (C_p) on the plate can be mathematically expressed as:

$$C_p = \frac{\rho V^2 S \sin^2 \alpha}{\frac{1}{2}\rho V^2 S} = 2 \sin^2 \alpha \tag{1}$$

Despite notable discrepancies observed between theoretical predictions and practical outcomes, Newtonian impact theory remains a valuable tool, particularly in simulating hypersonic flows. Tobak's pioneering work [10] emphasized the utility of this theory in determining dynamic derivatives from pressure coefficient data, thus highlighting its practical relevance.

Building upon Newton's original formulation, further refinements were introduced to enhance its predictive capabilities. Busemannn [11] incorporated centrifugal terms into the theory, leading to the development of the Newtonian–Boltzmann theory for calculating longitudinal dynamic derivatives of oscillating thin airfoils. Additionally, an embedded Newtonian flow theory, devised in 1962, expanded the theory's applicability, particularly in computing dynamic derivatives of hypersonic vehicles [12, 13].

This modified version of Newtonian impact theory offers a swift means of calculating dynamic derivatives by simplifying flow in the shock layer. However, its applicability is limited to scenarios involving relatively simple shock wave interactions. Nevertheless, these advancements underscore the enduring significance of Newton's impact theory and its derivatives in the realm of aerodynamic analysis, serving as invaluable tools in the pursuit of understanding complex fluid dynamics.

B. Piston Theory Based Method

Piston theory, as elucidated by Ashley in 1956 [14], represents a pivotal concept in aerodynamic analysis. Founded on the premise of high Mach numbers ($Ma^2 \gg 1$) and slender airfoils, the theory postulates minimal interference between points on the airfoil, linking pressure solely to downwash velocity at a given location. Through the integration of the impulse theorem and isentropic principle, the pressure $p_A(x, y, t)$ at the position (x, y) of the airfoil is formulated as:

$$p_A(x, y, t) = p_\infty \left(1 + \frac{\gamma - 1}{2} \cdot \frac{V_n(x, y, t)}{a_\infty}\right)^{\frac{2\gamma}{\gamma-1}} \tag{2}$$

This expression serves as the basis for deriving unsteady aerodynamic forces and moments, enabling the computation of dynamic derivatives. Piston theory has found broad application in evaluating the dynamic stability of various airfoils and delta wings.

Recognizing inherent limitations in the original theory, scholars have endeavored to refine and extend its applicability. Modified local piston theory, incorporating local speed variations, has emerged to address constraints related to angle of attack and airfoil thickness. This adaptation has proven particularly valuable in computing dynamic derivatives for supersonic and hypersonic configurations [15, 16].

However, it is important to acknowledge the inherent simplifications of the piston theory-based method, which limit its utility to rapid analyses of dynamic stability in supersonic and hypersonic regimes. Despite its effectiveness within these contexts, its applicability beyond remains restricted, representing a significant limitation.

V. Numerical Techniques

Fig.[1] depicts a flowchart illustrating modern numerical methodologies primarily directed towards solving the unsteady Euler or Navier-Stokes equations. These approaches play a pivotal role in computing unsteady aerodynamic forces and moments, thereby enabling the determination of dynamic derivatives. Over the last decade, advancements in these techniques have significantly enhanced their efficiency and accuracy, particularly in transitioning from time-domain to frequency-domain analyses.

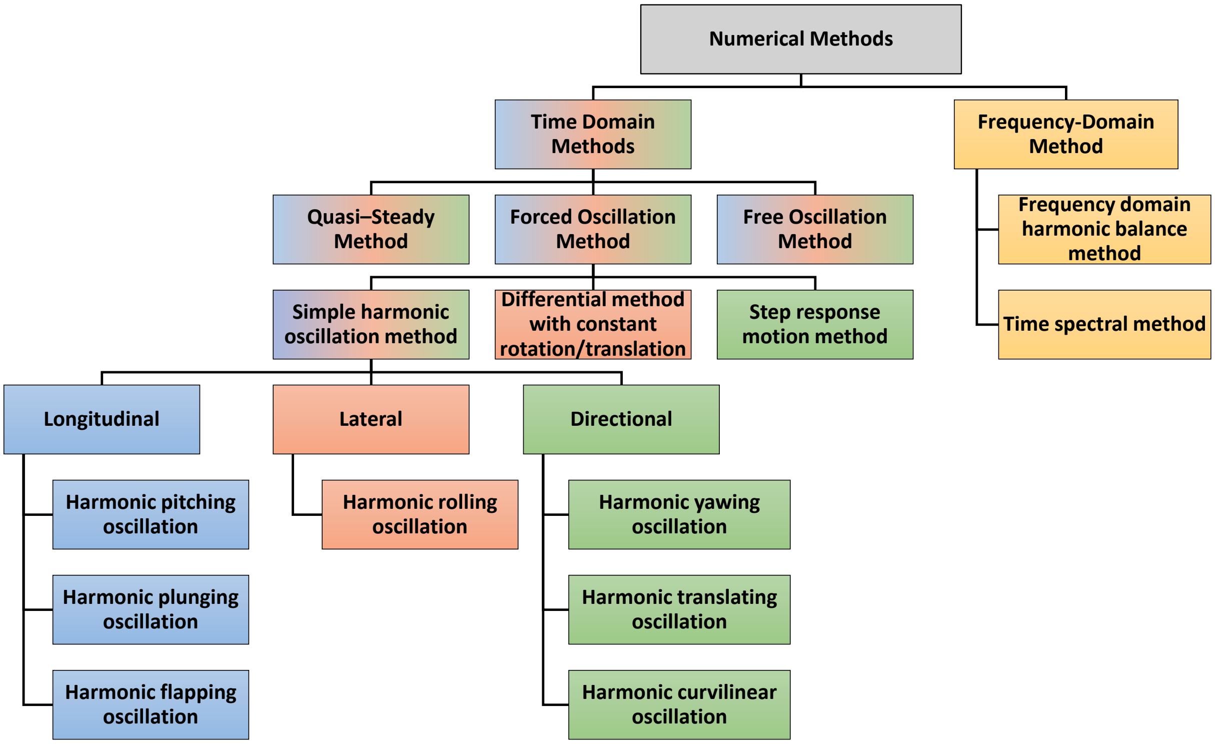
Numerical Methods
Time Domain Methods
Frequency-Domain Method
Quasi–Steady Method
Forced Oscillation Method
Free Oscillation Method
Frequency domain harmonic balance method
Simple harmonic oscillation method
Differential method with constant rotation/translation
Step response motion method
Time spectral method
Longitudinal
Lateral
Directional
Harmonic pitching oscillation
Harmonic rolling oscillation
Harmonic yawing oscillation
Harmonic plunging oscillation
Harmonic translating oscillation
Harmonic flapping oscillation
Harmonic curvilinear oscillation

Fig. 1 Block chain for modern numerical approaches

A. Time Domain approaches

Calculations in the time domain aim to ascertain various dynamic derivatives by analyzing the temporal characteristics of turbulent flow fields. Additionally, certain steady and quasi-steady methods tailored to specific scenarios are classified as temporal domain techniques. These include quasi-steady analysis, forced oscillation analysis, and free oscillation analysis, each differing in cost and complexity.

1. Quasi–Steady Method

Utilizing computational fluid dynamics (CFD) simulations, the quasi-steady approach is employed to derive dynamic derivatives. These methodologies solve steady governing equations within a non-inertial frame rather than an inertial frame. An exemplar of the quasi-steady technique for determining dynamic derivatives is the computation of the rolling-damping derivative C_{l_p}, which signifies the alteration in rolling moment per unit rolling rate. The imposition of a constant roll rate p on a systematic body at zero angle of attack sustains a consistent rolling moment.

$$C_l - C_{l_0} - C_{l_p}\frac{pc}{2V} = 0 \tag{3}$$

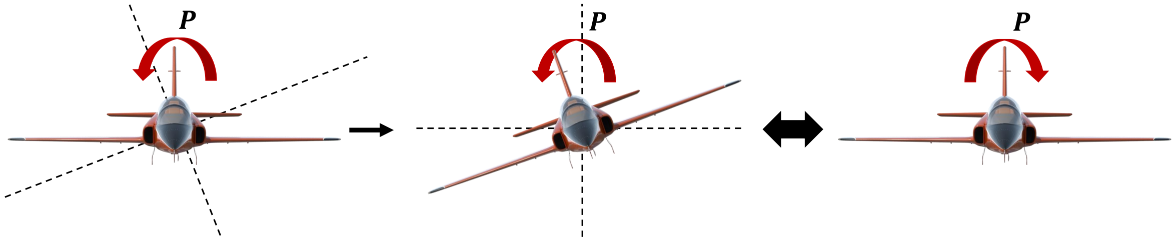

Fig. 2 Constant rolling at zero angle of attack

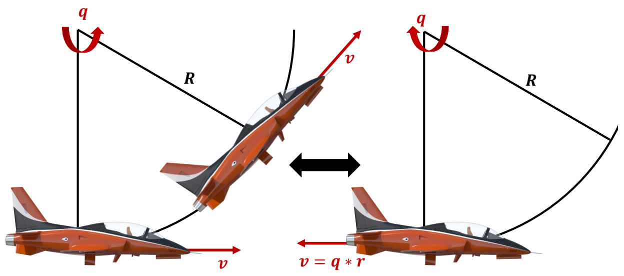

Fig. 3 Steady pull-up maneuver

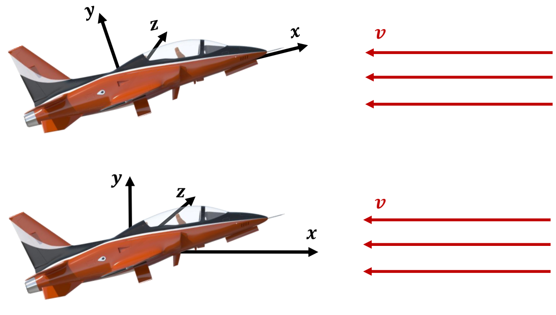

Fig. 4 Constant rolling at non-zero angle of attack

Fig.[2] illustrates the process of transforming dynamic motion into a coordinate system to maintain the body's position at rest. Aerodynamic forces and moments are computed through steady iterations, and C_{l_p} is derived using Eqn.(3) [17, 18]. This approach is applicable even for non-zero angles of attack. However, due to the quasi-steady characteristic being based on the wind axis system, the dynamic derivatives need to be transformed using Eqn.(4), as demonstrated in Fig.[3].

$$\begin{aligned} C^b_{lp} &= C^w_{lp}\cos^2\varepsilon - \left(C^w_{lr} + C^w_{np}\right)\sin\varepsilon\cos\varepsilon + C^w_{nr}\sin^2\varepsilon \\ C^b_{nr} &= C^w_{nr}\cos^2\varepsilon + \left(C^w_{lr} + C^w_{np}\right)\sin\varepsilon\cos\varepsilon + C^w_{lp}\sin^2\varepsilon \end{aligned} \tag{4}$$

where ε denotes the angle between the body and wind axes.

As illustrated in Figure 4, the quasi-steady approach can also be extended to determine the longitudinal-damping derivative C_{m_q}. A common motion associated with this derivative is the constant pull-up maneuver without elevator angle, wherein the aircraft maintains a stable rotation in the vertical plane while the velocity and angle of attack remain constant. By applying a constant pitch rate to the frame rather than the aircraft, the flow field can be readily converted to a steady case, allowing for the determination of damping derivatives using the quasi-steady approach. Utilizing the pitch rate q and radius R of the movement to maintain $V = qR$ at the center of gravity of the aircraft, the constant pitching moments C_{m_q} can be easily calculated.

The fundamental quasi-steady approach is capable of determining only the damping derivative of a symmetrical configuration. Park [19] introduced a universal method for computing all dynamic derivatives through constant computation.

In certain scenarios, the quasi-steady approach serves as a simpler calculation methodology. Initially, it was limited to calculating only the rotating derivatives of simple thin bodies. However, with the expansion of computational fluid dynamics (CFD) codes in non-inertial reference frames, the approach can now compute all dynamic derivatives. Despite its increased applicability, this technique has inherent limitations and cannot accurately represent nonlinear unsteady aerodynamics. Moreover, the precision of dynamic derivative calculations using this method is inferior to that of unsteady methods. Nevertheless, it remains a practical approach for establishing initial design parameters.

2. ***Forced Oscillation Method***

The forced oscillation method has been extensively utilized for computing dynamic derivatives [20, 21]. This technique involves extracting unstable aerodynamic data from various dynamic maneuvers, originating from dynamic wind tunnel tests. Known for its high precision and adaptability, the forced oscillation method yields favorable outcomes across subsonic, supersonic, and hypersonic regimes. Considered the most comprehensive approach for simulating dynamic derivatives in the time domain, it is also reliable for generating inputs for flight quality assessments.

However, the conventional forced oscillation technique primarily calculates integrated dynamic derivatives, which may be insufficient for sophisticated aircraft requiring precise aerodynamic and control system development with comprehensive individual dynamic derivatives. Consequently, several innovative methods have been developed and verified. In this study, we analyze the advantages and limitations of various forced oscillation methods.

2.1 Simple harmonic oscillation method The earliest form of dynamic derivatives encountered is the combined dynamic derivative, which serves as the primary focus of identification for most traditional approaches. This derivative is commonly estimated using a simple harmonic oscillation technique. Unsteady aerodynamics determined through computational fluid dynamics (CFD) tools can be utilized to derive combined dynamic derivatives [22], achieved by inducing simple harmonic motion in the aircraft's oscillation around its center of gravity. For instance, in longitudinally disturbed motion as depicted in Fig.[7], the aircraft undergoes oscillations about its center of gravity, leading to an instantaneous change in angle of attack given by:

$$\Delta\alpha = \alpha_m \sin(\omega t) \tag{5}$$

The coefficient of pitching moment can be represented as a function of $\Delta\alpha$ and q:

$$C_m = C_{m_0} + C_{m_\alpha}\Delta\alpha + C_{m_{\dot\alpha}}\Delta\dot\alpha + C_{m_q}\Delta q + C_{m_{\dot q}}\Delta\dot q + \hat\Delta(\Delta\alpha, q) \tag{6}$$

When the free stream remains constant, the pitching rate q is in the same form with $\Delta\dot\alpha$.

$$\begin{aligned} \Delta\dot\alpha &= \omega\alpha_m \cos(\omega t) = q \\ \Delta\ddot\alpha &= -\omega^2\alpha_m \sin(\omega t) = \dot q \end{aligned} \tag{7}$$

Since aerodynamics can be approximated as linear or weakly nonlinear for small or medium angles of attack, higher-order components can be neglected, simplifying the unsteady moment coefficient as follows:

$$C_m = C_{m_0} + C_{m_\alpha}\Delta\alpha + \left(C_{m_{\dot\alpha}} + C_{m_q}\right)\Delta q \tag{8}$$

Various methods, including the integration method, the least squares method, and the single-point method, can be employed to identify the combined dynamic derivative $C_{m_{\dot\alpha}} + C_{m_q}$. The integration method utilizes the area integral of the aerodynamic moment, providing an average result while considering the influence of time history. In contrast, the least squares method directly determines the coefficients by fitting the unsteady aerodynamic moment data. The single-point method relies solely on quasi-steady and occasionally unsteady aerodynamic moments to compute the dynamic derivative. Although straightforward, this method may yield significant inaccuracies in nonlinear situations.

The method of simple harmonic oscillation can also be applied to determine lateral combined dynamic derivatives, associated with simple harmonic rolling and yawing oscillations. Cross terms can be calculated by determining the cross unsteady aerodynamic moments using similar techniques. Enhancements to the standard simple harmonic oscillation enable more precise computations of dynamic derivatives. Fig.[8] illustrates the basic harmonic plunge oscillation [22]. In this technique, only the angle of attack is altered, and the unsteady aerodynamic moment remains unaffected by pitch rate, allowing for the determination of one of the single dynamic derivatives, $C_{m_{\dot\alpha}}$.

causing the aircraft to plunge as

$$h(t) = h_m \sin(\omega t) \tag{9}$$

During oscillation, the increased angle of attack can be stated as

$$\Delta\alpha \approx \frac{\Delta V}{V} = \frac{\omega h_m \cos(\omega t)}{V} \tag{10}$$

$$\Delta\dot\alpha = \frac{-\omega^2 h_m \sin(\omega t)}{V} \tag{11}$$

The Taylor expansion of the unsteady aerodynamic moment is refined by disregarding higher-order terms.

$$C_m = C_{m_0} + C_{m_\alpha}\Delta\alpha + C_{m_{\dot\alpha}}\Delta\dot\alpha \tag{12}$$

The pitching moment coefficient derivative due to angle of attack rate, $C_{m_{\dot\alpha}}$, can be determined using the same methodology as $C_{m_{\dot\alpha}} + C_{m_q}$. Additionally, the derivatives of directional acceleration, $C_{n\dot\beta}$ and $C_{l_{\dot\beta}}$, can be identified through translating oscillation. Apart from subtracting both the acceleration and combined derivatives, the simple harmonic oscillation technique provides an efficient approach for calculating the remaining damping derivative, C_{m_q}. As illustrated in Figure 9, the flapping motion [23] combines pitching and plunging oscillations without canceling the effect of angle of attack when determining C_{m_q}.

The additional attack angle induced by pitching oscillation is

$$\Delta\alpha = \alpha_m \sin(\omega t) \tag{13}$$

To counteract the effect of $\Delta\alpha$, the additional velocity must provide a negative $\Delta\alpha$ value.

$$\Delta V = -V\alpha_m \sin(\omega t) \tag{14}$$

The plunging oscillation is considered to be

$$h(t) = \frac{V\alpha_m}{\omega}\cos(\omega t) = h_m \cos(\omega t) \tag{15}$$

Similar to C_{m_q}, the directional-damping derivatives C_{n_r}, C_{l_r} are estimated with the coupled oscillations of translation and yawing [24].

Pioneering the application of resonance perturbation methodology for the quantification of dynamic derivatives, [25] introduced an innovative approach. This technique conceptualizes unsteady flow as a linear superposition of a pre-existing steady flow and minor perturbative flows induced by oscillations. These perturbations are approximated to Euler solutions, mirroring the initial steady-state flow, to simplify the computation process. Consequently, pitch damping derivatives are derived through the evaluation of aerodynamic moments, utilizing transformation formulas across different axes. In a collaborative effort, DLR and EADS-MAS developed a universal Unmanned Combat Air Vehicle (UCAV), named SACCON, featuring a blended delta wing-body configuration, to facilitate the validation of stability and control prediction algorithms (see Figs.[5] and [6]). Complementarily, NASA Langley and the German–Dutch Wind Tunnel (DNW) contributed to this endeavor by generating both static and dynamic wind tunnel data for the SACCON model using a low-speed wind tunnel. This collaborative effort utilized a variety of Computational Fluid Dynamics (CFD) algorithms to accurately model fluid dynamics, reflecting the complexities of flow physics [26, 27]. The National Research Council of Canada (NRC) introduced a calibration model for dynamic rotational and oscillatory testing, alongside numerical validation [28, 29]. This model is designed to generate steady vortices from the strake wing to mitigate flow separation over the delta wing, demonstrating the efficacy of CFD algorithms in simulating dynamic derivatives at transonic speeds. The Basic Finner Missile (BFM) model has been prevalently utilized as a dynamic derivative model due to its simplistic design and the extensive availability of wind tunnel test data. This model has long served as a benchmark for the assessment of CFD programs using the simple harmonic oscillation method [30–33]. Recent systematic research conducted by the European project SimSAC on the experimental and numerical determination of dynamic derivatives has showcased significant advancements [34, 35]. Utilizing the tiny harmonic oscillation approach, this project calculated the combined dynamic derivatives of two geometries: DLR-F 12 and a generic Transonic Cruiser (TCR), employing a spectrum of computational tools from linear aerodynamics (Vortex Lattice Method) to advanced CFD (Unsteady Reynolds-Averaged Navier–Stokes solver). Additionally, the dynamic derivatives of the F/A-18 and F-16 fighters were meticulously assessed, validating the practical efficacy of the simple harmonic oscillation method in simulating the aerodynamics of high-maneuverability aircraft [36, 37]. As illustrated in Fig.[10], the methodology for computing both longitudinal and lateral single, as well as combined dynamic derivatives using the simple harmonic oscillation method, is detailed, contributing significantly to the field of aerodynamic research.

2.2 Differential method with constant rotation/translation The motion of a flying vehicle in simple harmonic oscillation exhibits periodic behavior, wherein the computation of the unsteady state is essentially a reduction from the steady state. However, to ensure the periodic variation of aerodynamic forces and moments, it is imperative to simulate more than three harmonic oscillations, a process that can be notably time-consuming. To address this challenge, a

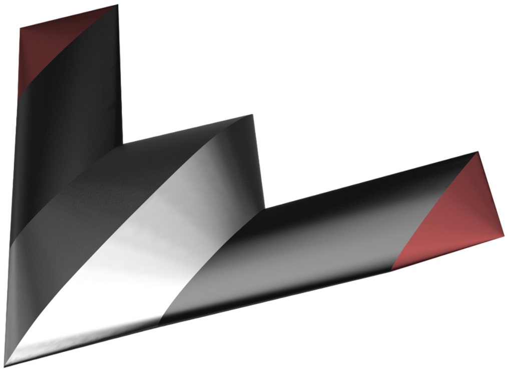

Fig. 5 SACCON shape

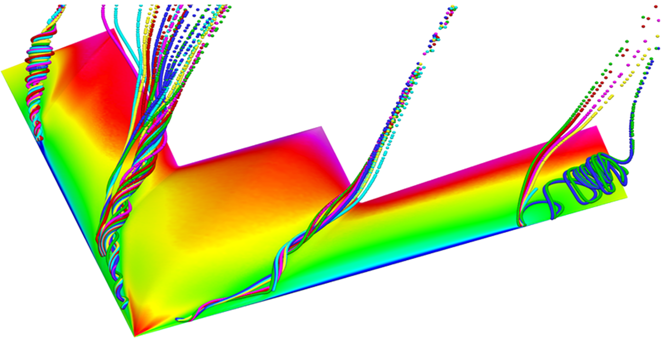

Fig. 6 SACCON CFD pressure and flow distribution

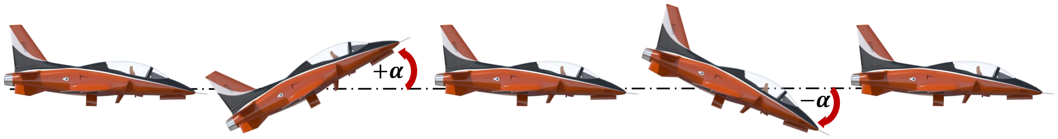

Fig. 7 Longitudinal simple harmonic oscillation

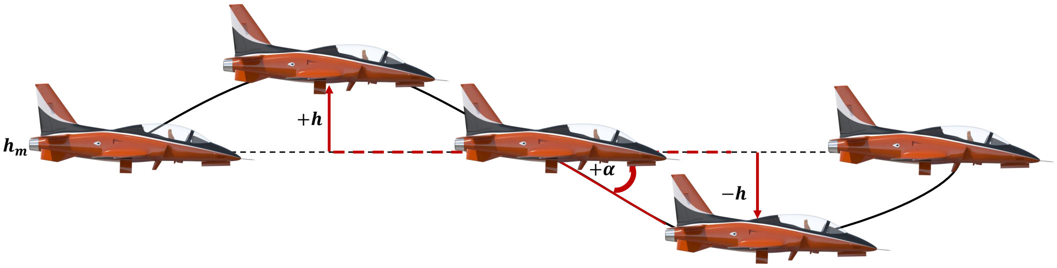

Fig. 8 Process of simple harmonic plunge oscillation

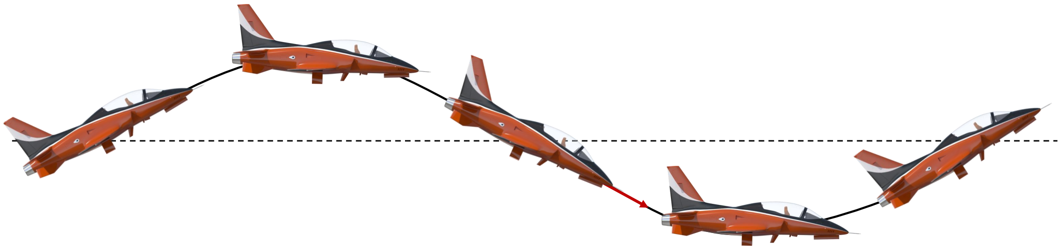

Fig. 9 Simple harmonic flapping oscillation

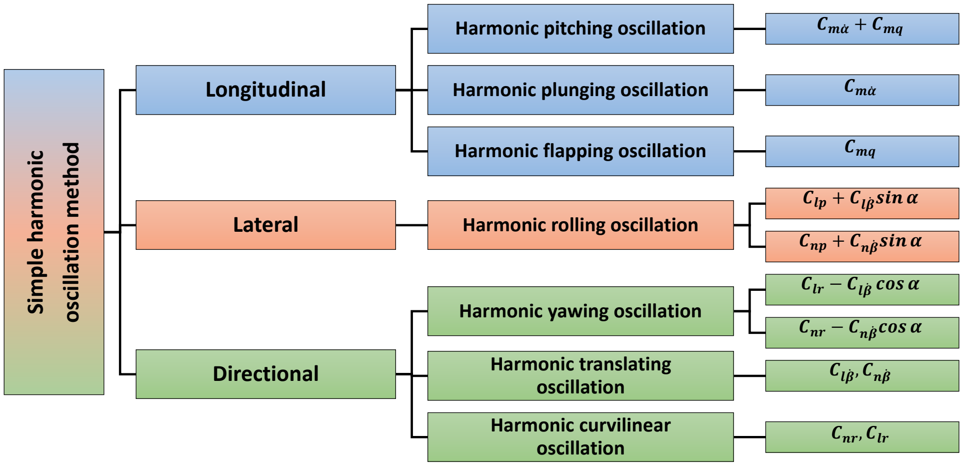
Simple harmonic oscillation method
Longitudinal
Lateral
Directional
Harmonic pitching oscillation
Harmonic plunging oscillation
Harmonic flapping oscillation
Harmonic rolling oscillation
Harmonic yawing oscillation
Harmonic translating oscillation
Harmonic curvilinear oscillation
$C_{m\dot{\alpha}} + C_{mq}$
$C_{m\dot{\alpha}}$
C_{mq}
$C_{lp} + C_{l\dot{\beta}} \sin\alpha$
$C_{np} + C_{n\dot{\beta}} \sin\alpha$
$C_{lr} - C_{l\dot{\beta}} \cos\alpha$
$C_{nr} - C_{n\dot{\beta}} \cos\alpha$
$C_{l\dot{\beta}}, C_{n\dot{\beta}}$
C_{nr}, C_{lr}

Fig. 10 Calculating dynamic derivatives with simple harmonic oscillation method

unique differential approach based on the disparity in the vehicle's forces and moments is proposed, offering an efficient means to compute both single and combined dynamic derivatives [22, 38].

The differential method employed for computing combined dynamic derivatives involves inducing constant pitching with two distinct pitch rates. As illustrated in Fig. [11], when altering the aircraft's pitch by $\Delta\alpha$ using pitch rates q_1 and q_2, the relationship between the additional angle of attack $\Delta\alpha$ and the pitch rates q is described as follows:

$$\begin{aligned} \Delta\alpha &= q_1 t_1 \\ \Delta\alpha &= q_2 t_2 \end{aligned} \tag{16}$$

During the pitching maneuver, the unsteady aerodynamic moments are obtained through Taylor expansion, which can be formulated as:

$$\begin{aligned} C_{m_1} &= C_{m_0} + C_{m_\alpha}\Delta\alpha + \left(C_{m_\alpha} + C_{m_q}\right) q_1 \\ C_{m_2} &= C_{m_0} + C_{m_\alpha}\Delta\alpha + \left(C_{m_\alpha} + C_{m_q}\right) q_2 \end{aligned} \tag{17}$$

Where C_{m_1} and C_{m_2} are the pitching moment coefficient due to angle of attack value α_1 and α_2 respectively. to compute the combined dynamic derivative, the following equation is produced by subtracting the two equations.

$$C_{m_{\dot{\alpha}}} + C_{m_q} = \frac{C_{m_1} - C_{m_2}}{\overline{q_1} - \overline{q_2}} \tag{18}$$

In contrast to the conventional simple harmonic oscillation method, the differential method does not involve periodic calculations, rendering it notably effective. However, it still operates on the premise of minor disturbances. Specifically, the additional angle of attack $\Delta\alpha$ induced by the pitch rate should align in magnitude with the amplitude of the harmonic oscillation. Application of the differential method for deriving combined dynamic derivatives involves continuous rolling or yawing motion during lateral simulation. Similarly, the modeling of acceleration derivatives, denoted as $C_{m_{\dot{\alpha}}}$, is based on the aerodynamic disparity resulting from constant plunging movements. By inducing the aircraft to translate to the same instantaneous additional angle of attack using two additional velocities derived from constant angle of attack rates $\dot{\alpha}_1$ and $\dot{\alpha}_2$, as illustrated in Fig.[12], the relationships between the incremental angle of attack and velocities are as follows:

$$\begin{aligned} \Delta V_1 &= V \tan\left(\dot{\alpha}_1 t_1\right) \approx V\dot{\alpha}_1 t_1 \\ \Delta V_2 &= V \tan\left(\dot{\alpha}_2 t_2\right) \approx V\dot{\alpha}_2 t_2 \end{aligned} \tag{19}$$

Using the principle of small disturbances, the unsteady aerodynamic moments are given as:

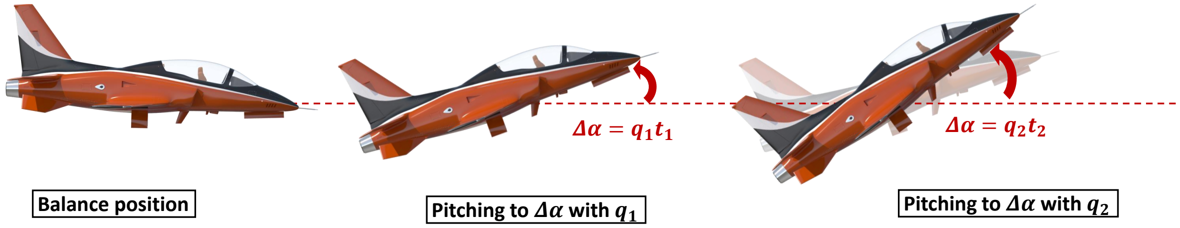
Balance position
$\Delta\alpha = q_1 t_1$
Pitching to $\Delta\alpha$ with q_1
$\Delta\alpha = q_2 t_2$
Pitching to $\Delta\alpha$ with q_2

Fig. 11 Combined dynamic derivative calculation with Differential method with constant rotation/translation

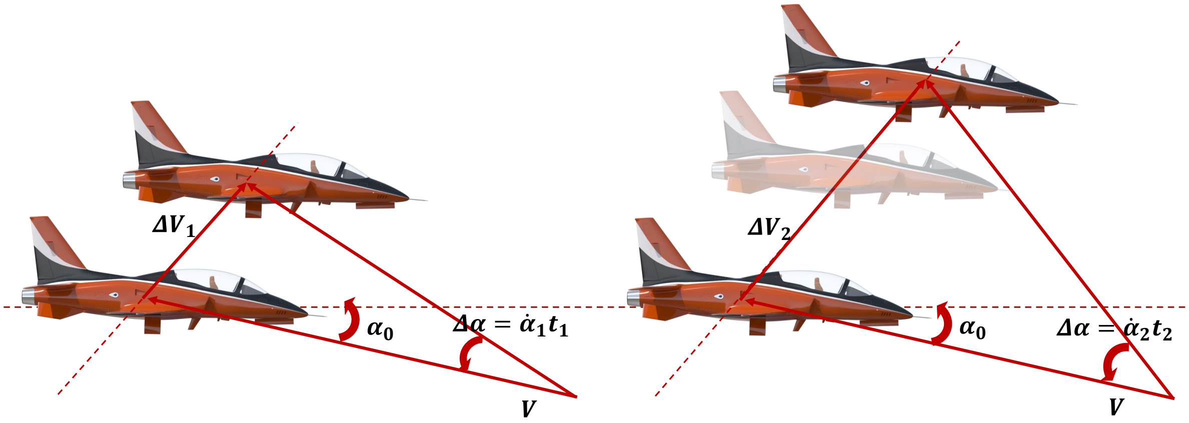
ΔV_1
α_0
$\Delta\alpha = \dot{\alpha}_1 t_1$
V
ΔV_2
α_0
$\Delta\alpha = \dot{\alpha}_2 t_2$
V

Fig. 12 Acceleration derivative identification with Differential method with constant rotation/translation

$$\begin{aligned} C_{m_1} &\doteq C_{m_0} + C_{m_\alpha} \cdot \Delta\alpha + C_{m_\alpha \cdot \dot{\alpha}_1} \\ C_{m_2} &\doteq C_{m_0} + C_{m_\alpha} \cdot \Delta\alpha + C_{m_\alpha \cdot \dot{\alpha}_2} \end{aligned} \tag{20}$$

Given that the additional angles of attack at final times are equivalent, the determination of $C_{m_{\dot{\alpha}}}$ can be achieved by subtracting the two corresponding equations.

$$C_{m_{\dot{\alpha}}} \doteq \frac{C_{m_1} - C_{m_2}}{\overline{\dot{\alpha}_1} - \overline{\dot{\alpha}_2}} \tag{21}$$

In addition to determining combination and acceleration derivatives, the rotational derivative C_{m_q} is also computed. Lateral variations in aerodynamic moments resulting from constant translations in the spanwise direction are utilized to calculate the single derivatives of C_{l_β} and $C_{n_{\dot{\beta}}}$. Compared to the conventional simple harmonic plunging oscillation method, the differential approach proves to be more efficient. This efficiency stems from the fact that acceleration derivatives are derived through simulations involving translations with two distinct angles of attack. It is noteworthy that an increase in computational time may lead to the emergence of additional angles of attack, potentially introducing numerical errors. Hence, it is imperative to estimate a suitable angle and calculation time before applying this approach.

2.3 Step response motion method Employing the differential approach, the derivation of a single dynamic derivative necessitates the execution of two constant movements. However, the complexity of this procedure underscores the need for a more systematic approach. In contrast to conventional methods, a novel technique rooted in step response motion has emerged, capable of computing both static and single dynamic derivatives in a stepwise manner. Fig.[13] elucidates the intricacies of this systematic technique [39, 40]. Furthermore, Fig.[14] depicts the relationship between the static derivative C_{m_α}, the acceleration derivative $C_{m_{\dot{\alpha}}}$, and the rotational derivative C_{m_q}, with respect to the angle of attack, rate of angle of attack, and pitch rate reaction movements, respectively.

The initial step involves executing the angle of attack reaction motion, wherein the flight vehicle is compelled to move with a constant additional angle of attack $\Delta\alpha$ to compute C_{m_α}. Given that only $\Delta\alpha$ influences the dynamic motion, the unsteady aerodynamic moment experiences an increase:

$$C_{m_1} = C_{m_0} + C_{m_\alpha} \cdot \Delta\alpha \tag{22}$$

The integration of unsteady and initial-steady aerodynamic moments facilitates the direct computation of the static derivative C_{m_α}.

$$C_{m_\alpha} = \frac{C_{m_1} - C_{m_0}}{\Delta\alpha} \tag{23}$$

Subsequently, the aircraft undergoes the rate of angle of attack response motion with $\dot{\alpha}$, inducing it to attain the same additional angle of attack $\Delta\alpha = \dot{\alpha}t$. The aerodynamic characteristics are solely governed by the variables $\Delta\alpha$ and $\dot{\alpha}$, expressed as:

$$C_{m_2} \approx C_{m_0} + C_{m_\alpha} \cdot \Delta\alpha + C_{m_{\dot{\alpha}}} \cdot \dot{\alpha} \tag{24}$$

The acceleration derivative is obtained by subtracting the ultimately unsteady moments C_{m_2} and C_{m_1} at the identical angle of attack $\Delta\alpha$.

$$C_{m_{\dot{\alpha}}} = \frac{C_{m_2} - C_{m_1}}{\bar{\dot{\alpha}}} \tag{25}$$

The determination of the rotary derivative C_{m_q} involves executing a consistent pitching motion with an identical additional angle of attack $\Delta\alpha = qt$. This dynamic process simultaneously integrates the influences of angle of attack and pitch rate, culminating in an unsteady aerodynamic moment.

$$C_{m_3} \approx C_{m_0} + C_{m_\alpha} \cdot \Delta\alpha + C_{m_{\dot{\alpha}}} \cdot \dot{\alpha} + C_{m_q} \cdot q \tag{26}$$

The derivation of C_{m_q} in conjunction with the rate of angle of attack response motion is outlined as follows:

$$C_{m_q} = \frac{C_{m_3} - C_{m_2}}{\bar{q}} \tag{27}$$

In comparison to conventional harmonic oscillation methods, the novel approach, characterized by simplified motion patterns, exhibits a reduction in computation times exceeding 60 percent. However, due to the approach's heightened sensitivity to the dynamic flow field, even minor nonlinearities can induce oscillations in aerodynamic forces and moments, consequently diminishing identification accuracy. Both traditional harmonic oscillation techniques and extended motion methods are classified as forced oscillation methods, governed by three primary parameters: frequency, motion rate, and amplitude. Among these, frequency holds particular significance in governing unsteady motion. When the reduced frequency is low, the reliable estimation of unsteady hysteresis becomes challenging, resulting in inadequate outcomes for dynamic derivatives or even sign reversals. Some scholars attribute this phenomenon to the aircraft transitioning from a dynamically stable state to an unstable state as the reduced frequency decreases to a certain threshold. Conversely, others contend that such outcomes stem from numerical simulation inaccuracies inherent to forced oscillation methods. Irrespective of the perspective, careful analysis of the specific computational model and optimal frequency selection are imperative to enhance numerical computation accuracy.

3. ***Free Oscillation Method***

The free oscillation method, derived from wind tunnel experiments for dynamic derivatives computation [41], presents an alternative approach. In this method, a rigid aircraft, subject to an initial instantaneous disturbance, undergoes oscillations about its fixed axis influenced by both the free stream and its inertia characteristics. Dynamic derivatives are then inferred from the resultant unsteady aerodynamic forces and moments utilizing computational fluid dynamics (CFD) software. In contrast to harmonic oscillation techniques, free oscillation more accurately reflects the essence of dynamic derivatives, showcasing the aircraft's ability to recover to its initial state post-disturbance. Incorporating inertia and mass values derived from empirical data, and with frequency and modal characteristics closely resembling those of the actual model, the single degree-of-freedom oscillation method obviates the need for reduced frequency selection inherent in harmonic oscillation methods, thereby enhancing the fidelity of flight simulations.

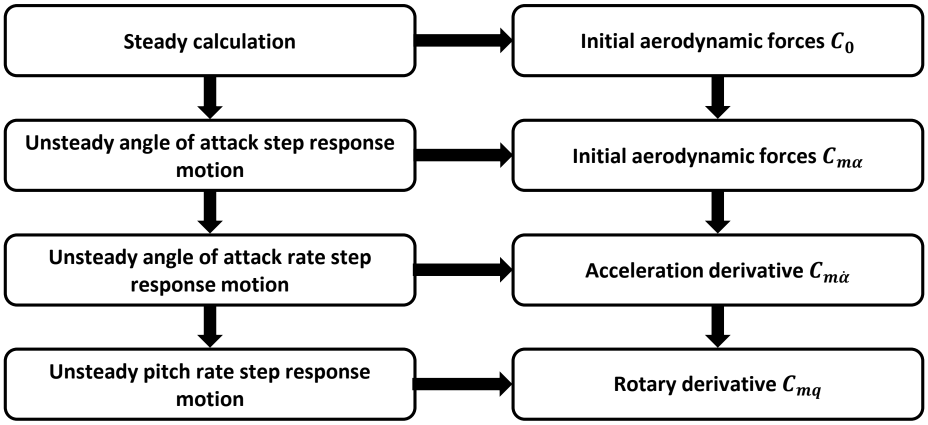
Steady calculation
Initial aerodynamic forces C_0
Unsteady angle of attack step response motion
Initial aerodynamic forces $C_{m\alpha}$
Unsteady angle of attack rate step response motion
Acceleration derivative $C_{m\dot{\alpha}}$
Unsteady pitch rate step response motion
Rotary derivative C_{mq}

Fig. 13 Detail calculating process of step response method

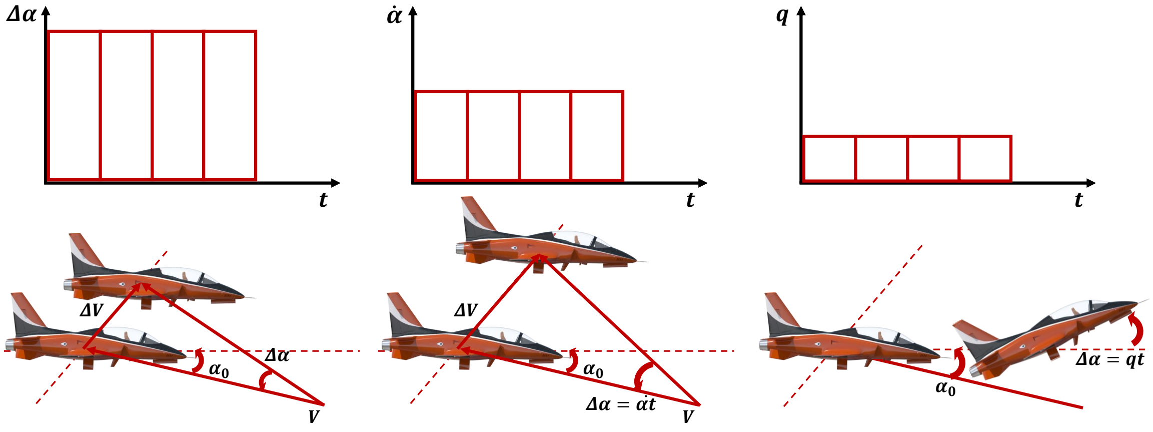

Fig. 14 Static and single dynamic derivatives calculation with step response method

Typically, oscillation with a single degree of freedom is employed to ascertain dynamic derivatives [42, 43], as illustrated in Fig.15. The free pitch maneuver involves granting lateral and directional freedoms, followed by applying angular pitch excitation to the aircraft, inducing longitudinal oscillation influenced by aerodynamics and inertias. The interplay between the aerodynamics and inertia of a flight vehicle during free pitch oscillation about a fixed axis is characterized by:

$$I_z\ddot{\theta} - n_z\dot{\theta} - C_m = 0 \tag{28}$$

Where, I_z, n_z and C_m are Moment of inertia to z axis, Damping coefficient and Ptitching moment coefficient respectively.

Once the free stream remains constant, the unsteady pitch moment is enlarged by eliminating higher order components, as follows:

$$C_m = C_{m_\alpha}\theta + \left(C_{m_q} + C_{m_{\dot{\alpha}}}\right)\dot{\theta} \tag{29}$$

So eqn.(28) will be:

$$I_z\ddot{\theta} - \left(n_z + \left(C_{m_q} + C_{m_{\dot{\alpha}}}\right)\right)\dot{\theta} - C_{m_\alpha}\theta = 0 \tag{30}$$

The combined-dynamic derivatives $\left(C_{m_q} + C_{m_{\dot{\alpha}}}\right)$ indicate the system's damping and define the oscillation mode. When $\left(C_{m_q} + C_{m_{\dot{\alpha}}}\right) < 0$, the reduced amplitude of the pitch moment represents dynamic stability; when $\left(C_{m_q} + C_{m_{\dot{\alpha}}}\right) > 0$, the rising amplitude indicates dynamic instability; and when $\left(C_{m_q} + C_{m_{\dot{\alpha}}}\right) = 0$, the amplitude will remain constant, indicating neutral stability.

The general solution to equation (28) takes the form $\theta = Ae^{\lambda t}\cos(\omega t + \varphi)$. By employing computational fluid dynamics (CFD) algorithms to model the aircraft's free pitch process, the time-history of the pitch moment is obtained, subsequently enabling the determination of combined dynamic derivatives. For instances characterized by small damping modes, $\left(C_{m_q} + C_{m_{\dot{\alpha}}}\right)$ can be approximated using instantaneous angles and times at the peak of oscillation. However, in cases of large damping or divergence, these values necessitate determination through the Moore–Penrose generalized inversion technique. The linear algebra approach known as the Moore-Penrose Pseudoinverse facilitates the estimation of the inverse for matrices that are not directly invertible. This technique enables effective computation of inverse approximations for matrices of various rectangular dimensions, regardless of squareness properties. Consequently, the Pseudo-inverse concept demonstrates its versatility, accommodating all conceivable matrix configurations. While the free oscillation method theoretically offers an accurate representation of dynamic derivatives and superior solution precision, practical implementation poses challenges. The unconstrained calculation process, primarily dictated by model inertia, may render CFD simulations more time-consuming compared to the harmonic oscillation method, potentially resulting in significant errors in dynamic derivative identification. Moreover, the restricted range of oscillation shapes limits the applicability of the free oscillation technique in calculating single and cross dynamic derivatives. These limitations have hindered the frequent utilization of the free oscillation approach in CFD simulations of dynamic derivatives.

B. Frequency Domain Methods

The primary drawback of the traditional harmonic oscillation approach with dual-time step lies in the computationally intensive periodic unsteady aerodynamic calculations, rendering it impractical for complex configurations. To address this, novel frequency domain approaches have been developed, integrating mechanisms for periodic aerodynamics of harmonic oscillation [44]. By leveraging multiple transient flow field solutions, it becomes feasible to reconstruct the entire unsteady flow field. Initially designed for turbine blades, these frequency domain techniques have demonstrated versatility in predicting flow characteristics around various aerodynamic structures, including rotor blades of helicopters [45], circular cylinders [46], and even aircraft flutter [47]. Frequency domain approaches can be categorized into linear and nonlinear types, with the latter being employed for dynamic derivative computations. Within the nonlinear realm, the harmonic balance method further subdivides into direct, time-domain, frequency, and splitting field methods [48]. Among these, the frequency domain harmonic method and time spectral approach serve as prominent techniques for calculating dynamic derivatives within the time domain harmonic balance method.

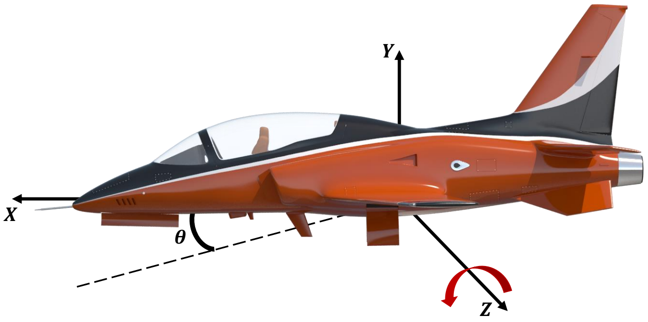

Fig. 15 Free pitch oscillation to calculate the longitudinal dynamic

1. *Frequency domain harmonic balance method*

The unsteady flow field expression is given by:

$$\omega D Q + R = \hat{0} \tag{31}$$

Let ω, R, and Q represent the angular frequency, flux vector, and conservative variable, respectively. The coefficient matrix D is defined as follows:

$$D_{i,j} = \frac{2}{N_T} \sum_{k=1}^{N_H} k \sin\left[2\pi k(j-i)/N_T\right] \tag{32}$$

Through Fourier transformation, the equation can be transformed into frequency domain representation by introducing a pseudo-time parameter E.

$$\hat{Q} = EQ \tag{33}$$

The time-domain solution Q for periodic unsteady flow is reconstructed from frequency-domain data.

$$Q(t) = \hat{Q}_0 + \sum_{n=1}^{\infty} \left[\hat{Q}_{cn}\cos(\omega n t) + \hat{Q}_{sn}\sin(\omega n t)\right] \tag{34}$$

The unsteady aerodynamic forces and moments for harmonic oscillation, based on the frequency domain harmonic balance method, are computed from data obtained at specified sample periods. Subsequently, dynamic derivatives are determined employing various methodologies. Moreover, the frequency domain harmonic balance approach can simulate both single and combined dynamic derivatives.

2. *Time spectral method*

The frequency domain harmonic balance method transforms the control equations of the unsteady flow field into the frequency domain and reconstructs the periodic aerodynamic forces using multiple sampling instances. Due to the complexity of transformations between time and frequency domains, the time spectral approach was developed [49, 50]. This approach inherits the excellent efficiency and precision of the frequency domain harmonic balancing method. Furthermore, all computations at sampling instances are directly performed in the time domain, eliminating the need for domain conversion. Consequently, the method is more practical for the analysis of periodic unsteady flow fields. The flow field variables undergo frequent fluctuations due to the harmonic oscillation of the flow field. To address this, the time period T of the unstable motion is divided into N equal parts, and the discrete Fourier transform (DFT) of the flow field variable w^n at time n can be calculated as follows:

$$\hat{w}_k = \frac{1}{N} \sum_{n=0}^{N-1} w^n \exp\left(-ik\frac{2\pi}{T} n\Delta t\right) \tag{35}$$

The inverse transformation is

$$w^n = \sum_{k=-\frac{N}{2}}^{\frac{N}{2}-1} \hat{w}_k \exp\left(ik\frac{2\pi}{T}n\Delta t\right) \tag{36}$$

The time derivative at n time is given as

$$D_t w^n = \frac{2\pi}{T} \sum_{k=-\frac{N}{2}}^{\frac{N}{2}-1} ik\hat{w}_k \exp\left(ik\frac{2\pi}{T}n\Delta t\right) = \sum_{m=-\frac{N}{2}}^{\frac{N}{2}-1} d_m w^{n+m} \tag{37}$$

$$\text{where } d_m = \begin{cases} \frac{2\pi}{T} \cdot \frac{1}{2}(-1)^{m+1} \cot\left(\frac{m\pi}{N}\right), & m \neq 0 \\ 0, & m = 0 \end{cases} \tag{38}$$

Equation (37) illustrates that the time derivative $D_t w^n$ can be analytically expressed as a function of w^n $(0 \leq n < N)$ at all sample times. Consequently, the governing equation is modified accordi

$$V\frac{\partial w^n}{\partial \tau} + VD_t w^n + R\left(w^n\right) = 0 \tag{39}$$

From the instantaneous aerodynamic forces and moments obtained through Equation (37) at the discrete sample times, the dynamic derivative is computed. Analogous to the frequency domain harmonic balance approach, the time spectral method enables the determination of both single and combined dynamic derivatives associated with harmonic oscillations. The frequency domain approach represents a streamlined methodology. By resolving the Fourier transformation of the governing equations, the periodic unsteady flow field is reconstructed using aerodynamic data at discrete sample times. However, this approach may entail a decrease in the accuracy of unsteady flow field calculations compared to the dual-time step technique due to the loss of important signal energy content. Consequently, the frequency domain approach may not sufficiently analyze detailed flow properties. For general linear problems, satisfactory approximations can be achieved with two or three sample points, leading to a doubling of computational efficiency compared to the dual-time step technique. However, employing more than five sample times to reconstruct periodic flow incurs a cost twice that of the dual-time step technique. Thus, the number of sample times dictates both the precision and efficiency of frequency domain techniques for calculating dynamic derivatives.

VI. Experimental Techniques

one undeniable truth prevails: Experimental Techniques stand as the epitome of reliability in data acquisition, notwithstanding their inherent challenges and substantial costs. In light of this, Fig.[16] serves as a comprehensive compendium, delineating the diverse spectrum of experimental methodologies employed for assessing aerodynamic derivatives. Through this elucidation, researchers gain invaluable insights into the myriad approaches available, guiding their endeavors towards a deeper understanding of aerodynamic phenomena.

A. Static Deflection

In the realm of experimental aerodynamics, the process of static deflection unfolds as follows: the model under scrutiny is securely mounted within the wind tunnel's test section, where it is subjected to a uniform and parallel airflow. The configuration of the model is meticulously tailored to align with the specific objectives of the test, encompassing both geometrically comparable and intentionally deformed variants. Within a predefined range of attack and sideslip angles, meticulous measurements of the forces and moments along the three-coordinate axes are conducted. These measurements furnish critical insights into the aerodynamic properties of the model, facilitating the determination of aerodynamic derivatives crucial for assessing the stability, control, and maneuverability of aerospace vehicles.

A.1 Similar geometrical models in straight parallel flow In this setup, the model is firmly affixed to the wind tunnel's test section, as illustrated in Fig. 17. The resulting forces and moments due to aerodynamic loading are carefully measured, accounting for the influence of wind tunnel boundary conditions. The obtained results are then presented as functions of attack and sideslip angles, as depicted in Fig. 19. The required derivatives are computed as the slopes of these relationships at the original position angles before any disturbance. For instance, lateral derivatives

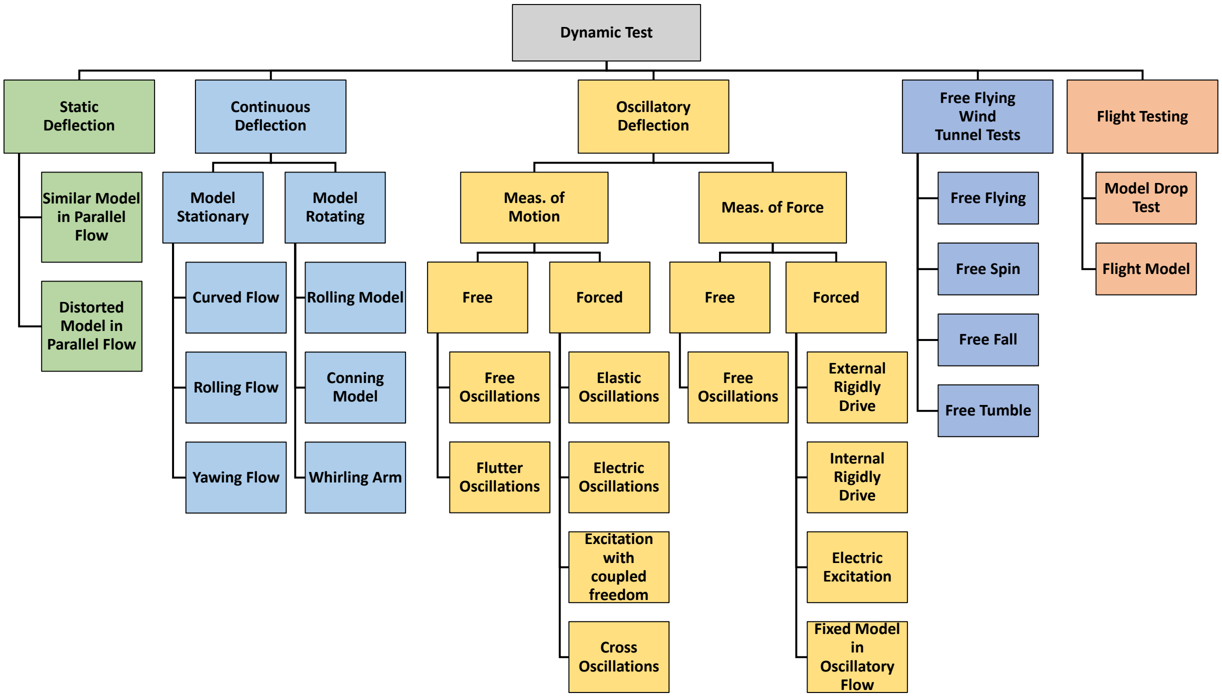

Fig. 16 **Experimental Techniques Flowchart for measuring dynamic derivatives**

are calculated as the mean value between equal and opposite values. Although the procedure is straightforward and uncomplicated, it is limited to deriving static derivatives exclusively.

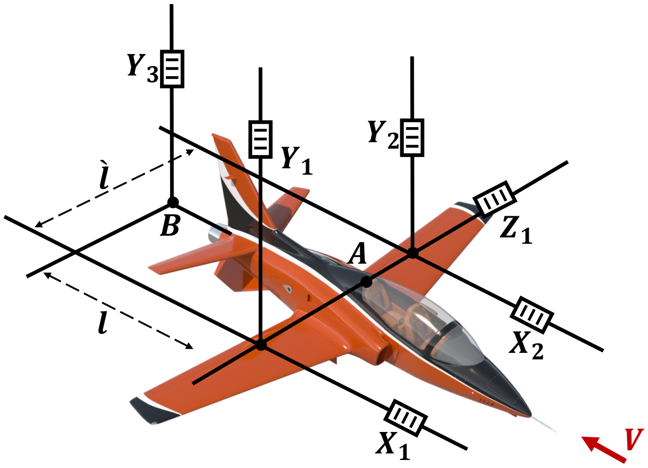

Fig. 17 **Model Suspension for Static Deflection Test**

A.2 Distorted geometric models in straight parallel flow As portrayed in Fig. 20, this approach involves subjecting a geometrically distorted model to straight parallel flow. The model is deliberately deformed to match the pressure distributions of a non-distorted model undergoing rolling, pitching, or yawing motions in parallel straight flow. Subsequently, standard six-component measurements are conducted, mirroring the procedure described in the preceding section. To illustrate this concept further, consider a plane with a lifting surface at zero angle of attack, a spanwise axis

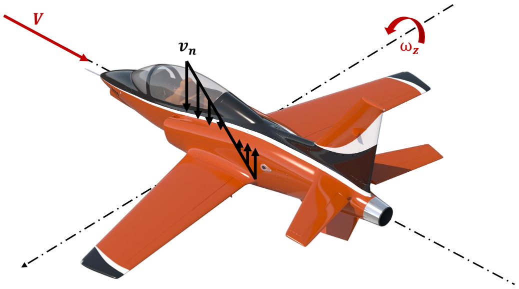

Fig. 18 Normal velocity distribution on wing in pitching motion

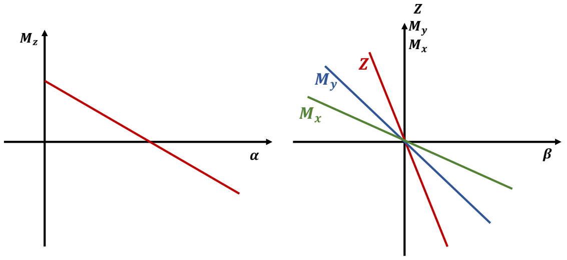

Fig. 19 Results of static deflection test

rotating with angular velocity q, and a wind speed of V, as depicted in Fig. 18. The wind velocity distribution normal to the wing is displayed, wherein a cambered wing with the same velocity distribution when at rest and flying in straight parallel flow V is evident. Leveraging the equivalence of normal velocities, the plane surface is replaced with one that is parabolically cambered. By adjusting the wind speed V while holding the value q/V constant, results for various pitch rates q can be obtained using a single model.

$$V\frac{\partial y}{\partial x} = -xq$$

integration with respect to x yields.

$$y = -\frac{1}{2}\frac{q}{V}x^2$$

The incorporation of a linear distribution of symmetrical twist serves as an additional means of model distortion, providing nearly identical pressure distributions over a wing in rolling motion. This innovative approach enables the measurement of dynamic derivatives on stationary models using static balances. However, a notable drawback is the necessity to fabricate and produce several complex and costly models.

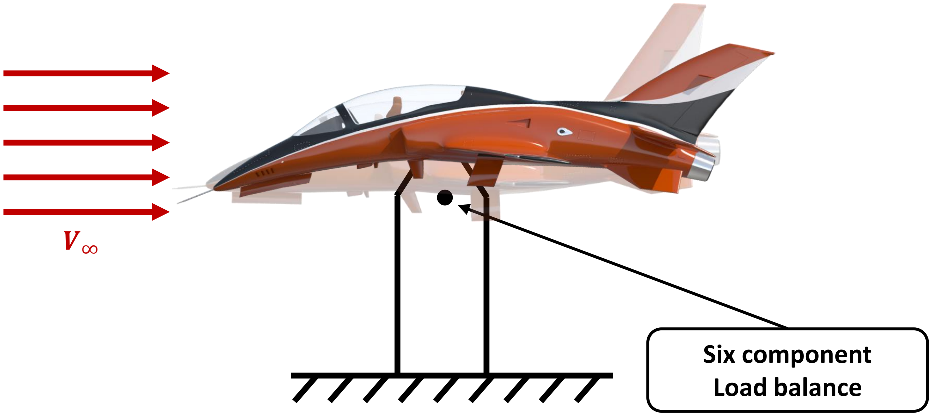

Fig. 20 Distorted Model in Parallel Flow

B. Continous Deflection

In this set of data, a relative continuous angular deviation is produced between the model and the airflow. It is achieved either by moving the model in a straight parallel flow or by flowing the stationary model in a curving or rolling flow.

B.1 Model Stationary (Curved Flow) Derivatives associated with pure yawing (C_{l_r}, C_{n_r}, and C_{Y_r}), as well as pure pitching (C_{m_q} and C_{L_q}), are determined by manipulating airflow using flexible walls, as depicted in Fig.[21]. The airflow velocity variation, proportional to the local stream curvature radius, is induced by upstream drag screens with decreasing density. The application of test sections with rotating or curved flow is typically limited to low-speed operations. An example is the NASA Langley 6 ft × 6 ft curved-flow test section, currently operational at Virginia Polytechnic Institute, which inherited the Langley stability tunnel in 1958 [51]. The curved-flow method involves emulating a steady curved-flight condition by utilizing a fixed model and configuring wind tunnel flow to curve around the model's vicinity. The flow curvature matches the model's curvature, with a velocity variation perpendicular to the streamlines directly proportional to the local curvature radius. This is achieved by employing flexible side walls to bend the flow and vertical-wire drag screens positioned upstream of the test section to create the necessary velocity gradient. The mesh size of these screens varies along the wind tunnel, with denser areas positioned at the inner radius of the curved test section. Pure yawing (due to r only) or pure pitching (due to q only) derivatives can be assessed using a fixed model mounted on a static balance. However, accurate modeling of steady curved flight presents challenges. Adjustments are often necessary for the buoyancy effect induced by the static-pressure gradient perpendicular to the streamlines, absent in curved flight. Additionally, differences in the behavior of the model boundary layer, which tends to migrate toward the center of curvature in curved flow, contrary to its usual tendency, and potential turbulence issues arising from relatively high turbulence levels behind the wire screen, must be addressed. Nevertheless, it is generally anticipated that these phenomena have only a modest impact on the measurement of purely rotary derivatives in most scenarios.

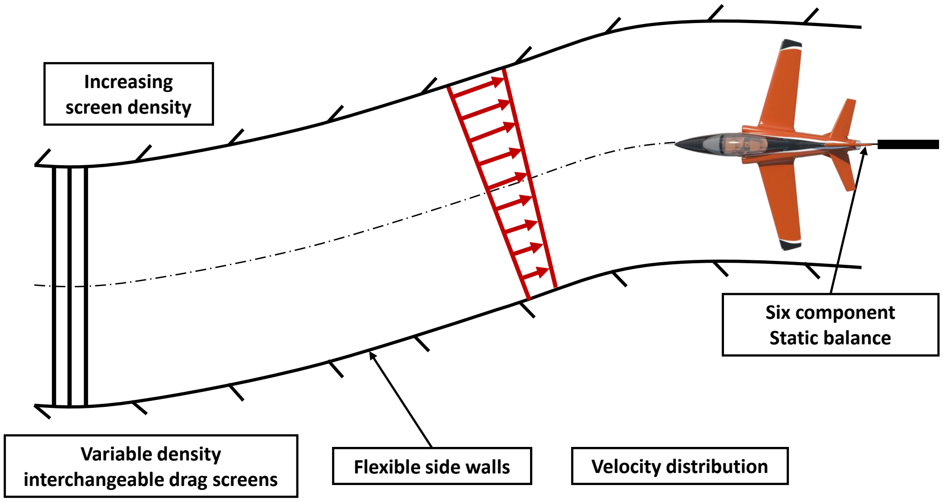
Increasing screen density
Six component Static balance
Variable density interchangeable drag screens
Flexible side walls
Velocity distribution

Fig. 21 Testing in curved flow

In its conventional configuration with straight walls, the curved flow test section measures 6 feet (1.83 m) square and 22 feet (6.7 m) in length. The vertical walls possess sufficient flexibility to conform to a curved shape, thereby inducing curved airflow around the model. Each vertical wall comprises 0.125-inch-thick (0.31-centimeter-thick) steel, segmented into three parts, with a 1-foot (0.30-meter) gap between sections for curvature adjustments. Adjustments to the curvature of the tunnel walls are made using a series of jack-screws positioned at regular intervals along the test section. The outer wall is pulled, while the inner wall is pushed into place, as predetermined [52]. To faithfully replicate a vehicle traversing a curved trajectory, two conditions must be met:

- The airflow must adhere to a circular path around the model vicinity.
- The velocity variation along the circular area streamlines must be directly proportional to the local radius of curvature of the flow.

This is accomplished by introducing wire screens into the flow upstream of the test section. Each custom-designed screen consists of a square steel frame with additional wooden elements for size adjustment. Vertically oriented stainless-steel wires extend from the bottom to the top of each screen, kept taut by tensioned springs. To ensure the appropriate total head and velocity gradient across the tunnel, the diameter and spacing of the wires vary across the screen. Wires are densely packed near the inner wall and spaced further apart near the outer wall. Each configuration of wall curvature corresponds to a specific arrangement of screens tailored to accurately replicate the corresponding flight conditions.

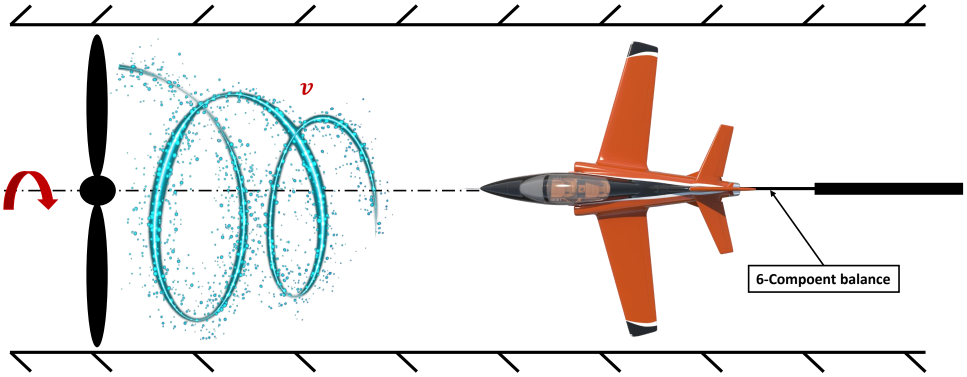

Fig. 22 Test section with rotary flow

B.2 Model Stationary (Rolling Flow) The airflow is redirected by a variable-speed rotor equipped with radially elongated blade chords, as illustrated in Figure 22. This configuration facilitates the measurement of continuous rolling derivatives (C_{l_p}, C_{n_p}, and C_{Y_p}). Notably, the testing conditions differ from those experienced by rolling the model itself. Centrifugal force induces a radial pressure differential in the surrounding air, thereby influencing the boundary-layer flow within the model. While the net effect of this gradient is nullified by considering the flow as potential and positioning the model symmetrically, variations become necessary when the boundary layer thickens due to yaw or incidence adjustments. When a model at an angle of attack rolls about a fixed body axis, the resulting aerodynamic responses depend on both the roll rate and the rate of change of the sideslip angle. To derive aerodynamic derivatives attributable to "pure" rolling, a stationary model submerged in a rolling flow is utilized. This facility is available at the Virginia Polytechnic Institute and State University, featuring a rolling-flow test section with a 6-foot diameter, in association with the former NASA-Langley stability tunnel [52]. To accurately replicate a pure roll maneuver, the rotational flow must be engineered such that the velocity component perpendicular to the tunnel axis increases proportionally with radial distance. Achieving this necessitates the deployment of a large rotor with nine specially designed vanes ahead of the test section, inducing a suitable solid core swirling motion within the flow. While the simulation of the pure roll maneuver may not be entirely precise, adverse effects are negligible for symmetrical models mounted symmetrically. However, in other cases, corrections may be warranted. The circular or "rolling flow" test section serves to simulate pure roll maneuvers. To achieve this, two key criteria must be fulfilled:

- The airflow must rotate around the model.
- The velocity component perpendicular to the tunnel axis must increase proportionally with radial distance from the centerline.

B.3 Model Rotating (Rolling model with parallel straight flow) The method is utilized to ascertain the damping in the roll derivative C_{l_p}. The model's rotation can either be unrestricted or tightly constrained. When the model rotates due to the deflection of its ailerons or fins, the resulting rolling velocity is determined. One advantage of this approach is its non-coercive nature. However, measuring rolling velocity poses challenges, and the underlying theory is similarly intricate. In the rigidly forced rotation method depicted in Fig. [23], the model undergoes continuous rolling while the reactive aerodynamic moment is measured using an appropriate balance. The derivative is then directly computed from the observed reactive moment and the imposed roll angular velocity.

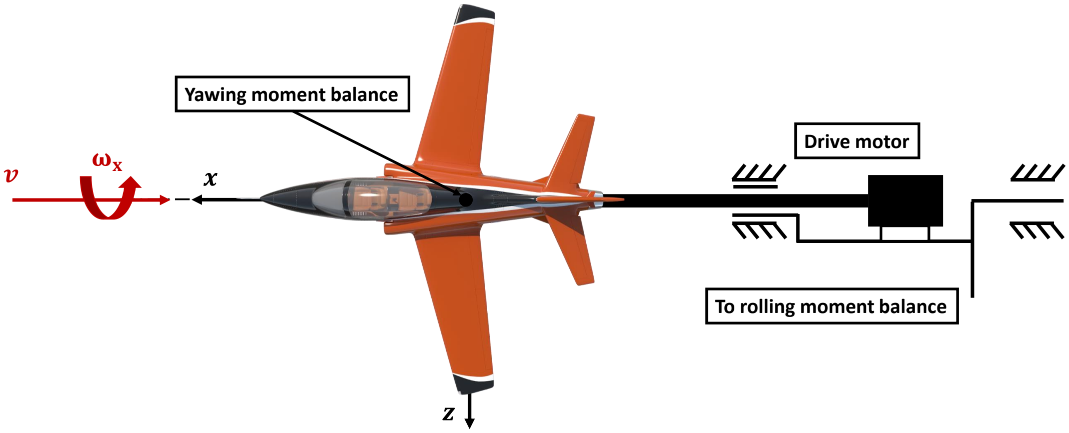

Fig. 23 Method of rigidly forced rotation

Furthermore, the cross derivative C_{n_p} can be obtained by situating a balance for measuring yawing moment at the origin of the coordinate system A. These methodologies bear resemblance to oscillatory techniques in principle. They are divided into constant roll (akin to forced oscillation) and free decay approaches (resembling free oscillation).

Figure [24] illustrates the configuration of a steady-state forced-roll apparatus designed for use in the NASA-Langley 7 x 10 Foot High-Speed Wind Tunnel. This apparatus is mounted on a six-component strain gauge balance, a type commonly used for the static testing of strut-supported models. The setup allows for variation in the angle of attack through replaceable connections between the balance and the rotating sting support. An internal hydraulic motor, characterized by constant displacement and reversible rotation, operates the model, necessitating adjustments in the recorded data to compensate for balance and support deflection under load, centrifugal force effects from these deflections, and any initial misalignment of the model's center of gravity (CG) with the roll axis [53].

For the testing of short-finned missile and bomb models in the 4-Foot-Transonic-Wind Tunnel, a free-decay roll apparatus has been developed. This apparatus incorporates a sleeve driven by a hydraulic motor and mounted on ball bearings atop a six-component balance. Models are mounted on this sleeve and can be accelerated to a predetermined spin rate; a pneumatically-operated clutch then disengages the drive motor, allowing models to spin freely on the bearings. During this free-spin phase, both spin rate and balance data are collected, with the drive system capable of delivering up to 138 lb.in of torque to the model at roll speeds reaching 5000 rpm [1]. The Department of Aerospace Engineering at the Middle East Technical University has undertaken measurements of the dynamic stability derivatives of a basic combat aircraft model undergoing oscillatory motion in roll. These experiments are conducted in the 8' x 10' low-speed, closed-circuit Ankara Wind Tunnel (AWT). The "Standard Dynamic Model (SDM)" employed is widely used across several NATO experimental facilities for wind-tunnel experiments. This model was developed and fabricated as part of a NATO AGARD Working Group (WG16) project. A five-component internal strain gauge balance measures the aerodynamic loads on the model, and the small-amplitude direct forced oscillation method is applied to analyze the balance's signal output. This approach offers a reliable means of calculating fundamental dynamic stability derivatives without the need to solve the equations of motion directly. The existing servo mechanical system in the Ankara Wind Tunnel (AWT), initially developed for pitch plane oscillations, is described [54]. This method was later adapted to facilitate oscillations in the roll plane [55], allowing for the measurement of both static and dynamic derivatives of the SDM using the forced oscillation technique.

B.4 Model Rotating (Conning) In recent developments, the study of aerodynamic phenomena associated with the rotational motion of aircraft has garnered increasing interest. It has been established that a comprehensive formulation of the motion equations, accounting for the nonlinear interactions among pitch, yaw, and roll, is essential. Within this refined formulation, a notable factor influencing the total aerodynamic moment is the rotary or coning motion. To accurately simulate this motion within a wind tunnel environment, the model is attached to a rotational balance. This balance's axis aligns parallel to the wind tunnel's centerline, fixed at a certain incidence and sideslip angle [56]. Theoretically, by slightly adjusting the axis of a rotary balance, it is possible to superimpose oscillatory pitch or yaw motions on the primary rotation. Nevertheless, the precision achievable through such adjustments, and whether it

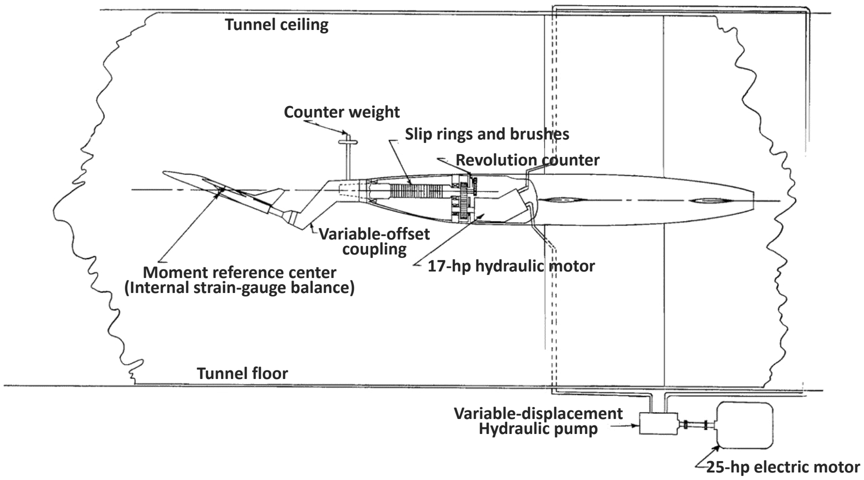

Fig. 24 General arrangement of forced-roll apparatus [53]

suffices for accurate measurement of pitching and yawing derivatives, remains uncertain. Rotary balance data play a crucial role in the development of forced oscillation capabilities within the rotary balancing framework. These capabilities are intended to explore subsonic rate damping characteristics, enhance spin predictions, and integrate spin modeling into comprehensive six-degree-of-freedom (6-DOF) simulations, facilitating the examination of "combined motion" or "oscillatory coning."

The rotational balance apparatus at NASA-Langley's Full-Scale Tunnel can provide six-component measurements across a range of attack angles from (45° ∼ 90°) and at a Reynolds number up to 3×10^6 at low speeds. This setup accommodates large-scale models and supports flying test methodologies, such as drop model techniques. Consequently, it enables the acquisition of aerodynamic data at Reynolds numbers comparable to those in actual flight tests. This data, in conjunction with conventional static force measurements, serves as input to theoretical spin prediction models for comparison against flight test outcomes [57]. NASA Langley also offers a refined rotary balance for experiments with 1:5 scale models within the Spin Tunnel, capable of reaching up to 90 rpm in either direction. This corresponds to a nondimensional spin rate of 0.9, with the attack angle range extending from 0 to 90 degrees [58]. The NASA-Ames rotating balance, designed for the 12-foot pressure and 11-foot transonic tunnels, enables remote adjustment of attack and sideslip angles. The use of bent stings and upper-mounted versions allows for an extended range of attack angles up to 100 degrees and sideslip angles to 25°, with a maximum spin rate of 400 rpm [59].

Rotary balance testing in the NASA Langley Research Center's 20-foot Vertical Spin Tunnel (VST) involves spinning the aircraft model at varying angular velocities, attack angles, and sideslip angles, utilizing an internally mounted six-component strain gauge balance for force and moment measurements. Test procedures typically adjust the angular velocity for each attack angle while maintaining a constant sideslip angle, employing both positive (clockwise) and negative (counterclockwise) angular velocities for comparative and validation purposes [60]. Given the impracticality of using a vacuum to determine the model's mass and inertial effects, "tare" measurements are conducted with the model enclosed in a large "tare bag" in the absence of airflow. This procedure is replicated for each combination of attack angle, sideslip angle, and angular velocity, with the tare bag ensuring that the surrounding air matches the model's rotational speed, thereby negating wind-off aerodynamic effects. For rotary testing, the aircraft model undergoes rotation and radial translation within the wind tunnel to maintain a constant spin axis relative to its center of gravity across all tested attitudes. This involves rotating the object at specified angular velocities, starting from zero and increasing through positive values before decreasing through negative ones. The test encompasses sideslip angles from -5 to 10 degrees and attack angles from 0 to 50 degrees, with reduced angular velocities ranging from -0.5 to 0.5 for attack angles exceeding 10 degrees. Control surface deflections are analyzed for sideslip angles of -5, 0, and 10 degrees.

C. Oscillatory Deflection

In a rigorously structured investigation, a model with comparable geometrical stiffness is subjected to oscillations within a parallel flow regime. The examination of motion records, or response patterns, facilitates the quantification of

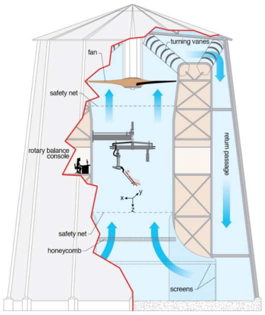

Fig. 25 Cross-section of the 20-Foot Vertical Spin Tunnel

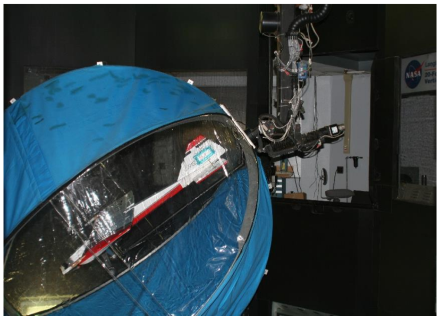

Fig. 26 FASER inside the rotary tare bag

both stiffening and damping derivatives amidst oscillatory behavior. This methodology is instrumental in ascertaining the damping characteristics pertinent to both pitch and yaw motions. Given the dynamic nature of the angle of attack over time, where $\frac{d\alpha}{dt} \neq 0$, the equivalence of $C_{m_{\dot\theta}} \neq C_{m_q}$ to the corresponding rotational derivative is not straightforward. The derivative $M_z^{\dot\theta}$ cannot be solely attributed to pure pitch actions. Rather, it is expressed as

$$C_{m_{\dot\theta}} = C_{m_q} + C_{m_{\dot\alpha}}$$

highlighting the necessity of an alternate approach for isolating C_{m_q}, particularly in scenarios where $\dot\alpha \neq 0$.

Traditional separation techniques often neglect the influence of both the wing and fuselage on $C_{m_{\dot\theta}}$. A refined analysis suggests that

$$C_{m_{\dot\theta}} = C_{m_{\dot\theta_{wb}}} - C_{m_{\dot\theta_{\text{tail}}}} \doteq C_{m_{\dot\theta_{\text{tail}}}}$$

revealing that, upon discounting the inherently unstable lift characteristics of the tail and considering solely its contribution to downwash lag, the tail's impact on drag is effectively nullified.

Furthermore, the relationship

$$C_{m_q} = \frac{C_{m_{\dot\theta}}}{\left(1 + \frac{d\mathcal{E}}{d\alpha}\right)}$$

is introduced, where $\frac{d\varepsilon}{d\alpha}$ denotes the rate of downwash angle change at the tail relative to the aircraft's angle of attack. Techniques for determining $\frac{d\varepsilon}{d\alpha}$ are discussed in detail within the literature.

The assumption of minimal wing-body interaction holds for configurations involving short fuselages and straight wings. However, this assumption becomes less valid with significantly swept or delta wings and elongated fuselages, particularly within low-speed regimes. The derived pure derivatives, as determined through previously outlined methods, are valid within this specific speed range, considering only the effects of the wing and body.

The exploration of the body's contribution to these dynamics presents an avenue for future research endeavors.

C.1 Measurement of Motion The determination of stiffness and damping derivatives is achieved through the analysis of motion records employing a temporal scale.

C.1.1 Free Motion (Free oscillation) Initial perturbation is introduced into an elastically constrained model shown in Fig.[27]. The oscillations that are decaying are examined. It is possible to write that assuming minimal deflections and disregarding higher order derivatives of aerodynamic moment. Eqn.(40) has a solution expressed as:

$$I_{zz}\dot\theta + k_\theta\dot\theta + \sigma_\theta\theta = C_{m_{\dot\theta}}\dot\theta + C_{m_\theta}\theta \tag{40}$$

assuming minimal deflections and ignoring higher order aerodynamic moment derivatives. Eqn.([**?**]) has a solution expressed as

$$\theta = \bar\theta e^{\lambda t} \tag{41}$$

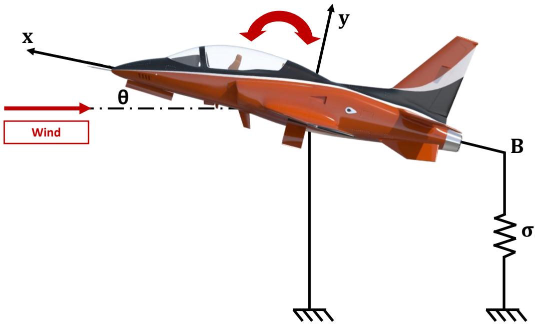

Fig. 27 Free oscillation method

Where,

$$\lambda = \mu + jp \tag{42}$$

When replacing by eqn. (41) and (42) in eqn.(40) and splitting into real and imaginary yields the following derivative expressions:

$$C_{m_\theta} = \sigma_\theta \left(p^2 + \mu^2\right) I_{zz} \tag{43}$$

From the frequency $f = \frac{p}{2\pi}$ and the logarithmic decrease $\delta = -\mu/2f$, the motion record values p and μ are derived. Total moment of inertia I_{zz}, the apparatus damping coefficient k_θ, and the elastic stiffness for angular displacement about the axis σ_θ are explained deeply in [61]. The first impetus might be provided by:

1) Mechanically.
2) Release from a displaced position.
3) Electrical stimulation at phase resonance with abrupt circuit break.

Methods 1, 2, and 3 adjust the amplitude of the initial impulse. Method 3 is appropriate for testing at high frequencies if the employed springs have a high elasticity. As there is only one degree of freedom in the motion, there is only one equation of motion involved. Thus, the analysis of outcomes is simplified. The record is unnecessary when using contemporary instruments to measure the rate of decay and frequency. The accuracy of derivative determination is then comparable to or even greater than that of previous approaches. The results of the method "decaying oscillations" don't indicate a discrete amplitude value, but rather an amplitude range. This amplitude range may be made very tiny with contemporary instruments so that findings as a function of amplitude can be obtained. the same as constant amplitude techniques. This is necessary when situations involving minor nonlinearities are of interest. Probably the oldest and simplest technique for determining oscillatory derivatives.

C.1.1.1 Free Motion (Free oscillation) (Single degree of freedom) The University of Bristol has created a specialized single-degree-of-freedom pitch-axis dynamic wind tunnel rig [62], resembling a 1/16th scale BAe Hawk model made mainly from fiberglass-coated wood. It boasts specific dimensions and employs aluminum gimbals for oscillation in five degrees of freedom, incorporating precise feedback systems for angular position and velocity. Experiments focused on inverted pitch motion, with a moment of inertia of 0.0343kg.m^2. Data collection utilized a DSPACE DS1103 system, MATLAB/Simulink, and Real-Time software, operating at a $100Hz$ sampling rate. The wind tunnel featured a $1.1m$ diameter, $40m/s$ maximum speed, and 1.5% turbulence at $20m/s$, with experiments conducted at the latter speed, corresponding to Re $= 0.2 \times 10^6$ based on the model's wing chord.

NASA Langley Research Center conduct a test at 14-by-22-Foot Subsonic Tunnel using the forced oscillation rig [63] shown in Fig.[28]. The model is mounted so that allow three angular oscillations motion roll, yaw, and pitch movements. The test rig consists of a motor and a gearbox that drive a flywheel. There is a vertical push rod that connects the flywheel to a crank then attached to a sting. The sting is attached to the model by an internally mounted 6-component strain gauge balance. The RPM of the motor can be adjusted to control the frequency of the oscillation the values can be varied between (0.1 to 1.0 Hz), and the radial location on the flywheel that the pushrod is mounted can be adjusted to set the oscillation amplitude the values can be varied (up to 30 degrees). For yaw oscillation the setup is the same as that for the roll ,but the sting in this case is attached through the upper or lower of the model. For pitch oscillation the flywheel is attached to another oscillation mechanism using a yoke arrangement to mount the balance, the pushrod rotates the balance with model about the pivot point on the yoke.

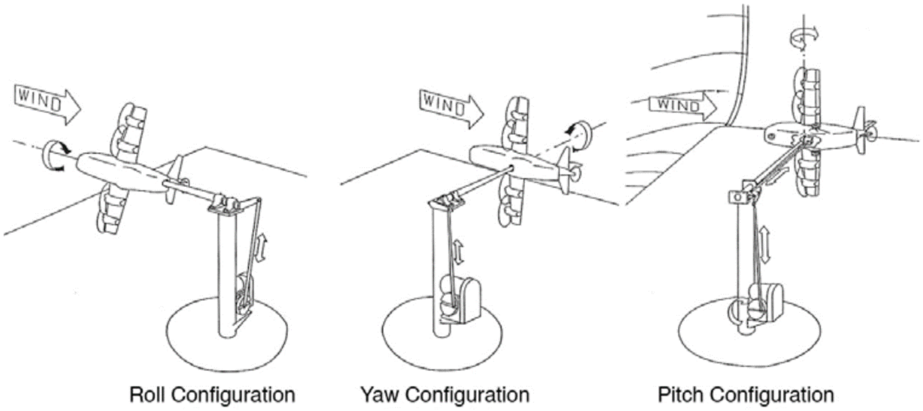

Fig. 28 NASA Langley Research Center 14-by-22-Foot Subsonic Wind Tunnel forced oscillation capability [63]

C.1.1.2 Free Motion (Free oscillation) (4-degree of freedom) Department of Aerospace Sciences in Cranfield University developed a 4-DOF test rig [64, 65], that consists of a vertical rod is supported by bearings at its upper and lower ends, allowing it to spin about its vertical axis. The rod is held in a massive, transportable Dexion structure by bearing mounting plates to which it is rigidly linked by wire bracing. The entire assembly, including the model as shown in Figures [29],[30], can be removed from the wind tunnel as a modular mechanism. A sleeve is keyed to the vertical rod so that it can glide freely vertically but must rotate with the rod. The sleeve is then incorporated into the model's suspension gimbal. The model can thus spin in pitch and roll about the sleeve; rotation in yaw revolves around the rod's vertical axis, and vertical translation includes the sleeve sliding on the rod. Potentiometers sense angular motion in each axis, which is restricted to 30 degrees. Vertical motion has lately been increased to approximately 0.75 m and is also detected using a potentiometer in a pulley-and-cable configuration. To reduce the model's reliance on the suspension system, the gimbal-and-rod assembly was designed as tiny and light as possible. To reduce friction, all rotating bearings have small precision ball races, and the sliding sleeve has precision linear ball bearings. To reduce impact damage when the model flies to the end stops, coil springs are added to the upper and lower ends of the vertical rod.

C.1.1.3 Free Motion (Free oscillation) (5-degree of freedom) The University of Bristol conducted a 5-DOF test rig [66–71], it comprises of a flight vehicle model attached to an arm by a two-degree-of-freedom gimbal. This arm is attached to the supporting framework via a three-degree-of-freedom gimbal. An aerodynamic compensation device is positioned on the downstream end of the arm to provide heave and sway aircraft model motions and correct for the mass,

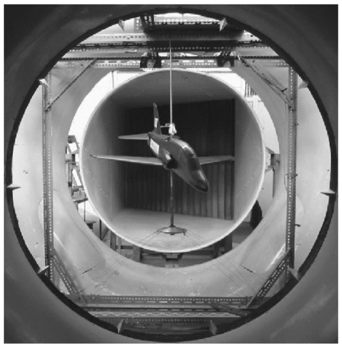

Fig. 29 4-DOF Dynamic wind-tunnel rig with a one-twelfth scale BAe Hawk

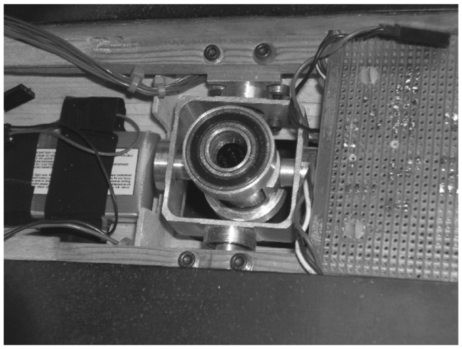

Fig. 30 4-DOF Dynamic wind-tunnel rig gimbal mechanism

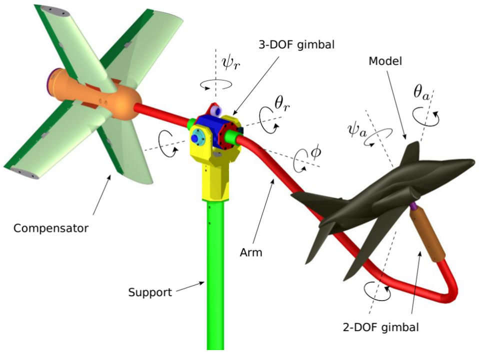

Fig. 31 The 5-DOF manoeuvre rig

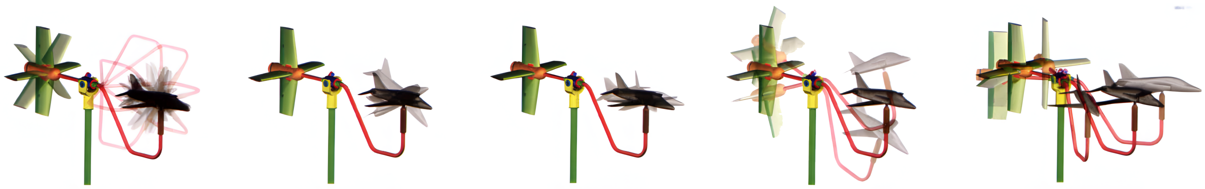
(a) Roll (ϕ) (b) Pitch (θ^a) (c) Yaw (ψ^a) (d) Heave (θ^r) (e) Sway (ψ^r)

Fig. 32 Illustration of the 5-DOF

inertia, and aerodynamic effects of the supporting arm, Fig.[31] depicts the manoeuvring rig and Fig.[32] shows the five available DOF. Because of the weight of this compensator, the pendulum can be statically balanced in the horizontal position. All axes of motion are lockable for situations where all five degrees of freedom are not required. The aircraft model must have its own actuating control surfaces and should ideally be dynamically scaled in order to be used on this rig. This is done so that it can be ’flown’ on the arm as closely as possible to the behaviors of the full-scale aircraft. The motions of this type of rig can be highly nonlinear, necessitating a sophisticated mathematical description to separate out the impacts of the rig dynamics. A mathematical model is described to that goal. It is based on the Lagrange formulation with constraints, resulting in a system of differential-algebraic equations. Terms that account for friction losses in the gimbals are a significant addition to this model. A minor modification has also been made to allow for scenarios where the flight vehicle model’s center of gravity (c.g.) does not lie on the pivot point.

C.1.2 Free Motion (Flutter oscillation) From the solution of flutter equations, the derivatives are calculated shown in Fig.[33]. The model is hung in a manner that causes flutter oscillations. The properties of flutter (wind speed and frequency under conditions of fully developed flutter) are measured. The system depicted in the diagram possesses two degrees of freedom [61]. The motion during stable flutter may be represented as:

$$I_{zz}\ddot{\theta} + k_{\theta}\ddot{\theta} + \sigma_{\theta}\theta + I_{yz}\ddot{y} = C_{m_{\dot{\theta}}}\dot{\theta} + C_{m_{\theta}}\theta + C_{m_z}\dot{y} + C_{m_y}y \tag{44}$$

$$C_m\ddot{y} + k_y\dot{y} + \sigma_y y + I_{yz}\ddot{\theta} = C_{L_{\dot{\theta}}}\dot{\theta} + C_{L_{\theta}}\theta + C_{L_{\dot{y}}}\dot{y} + C_{L_y}y \tag{45}$$

The motion can be presented as follows:

$$\begin{aligned} \theta &= \bar{\theta}e^{jpt} \\ y &= \bar{y}e^{j(pt+\varepsilon)} \end{aligned} \tag{46}$$

where $\bar{\theta}, \bar{y}$ represent amplitudes and represents phase shift. Four equations comprising the eight derivatives are constructed by substituting eqns (46) into (44) into real and imaginary terms. Repeating the test with different spring stiffness yields a new set of four equations. From the eight equations, the eight necessary derivatives are derived. At stable amplitude of oscillation, the derivatives are measured. Obtaining a comprehensive set of derivatives. employing no excitation. In fact, it is challenging to achieve steady limit cycle oscillations using this strategy. Additionally, when

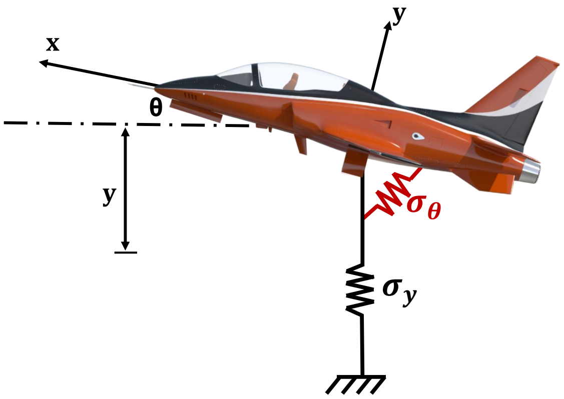

Fig. 33 Flutter oscillation method

derivatives are greatly influenced by wind speed. (In the transonic range) the results cannot be relied upon. This is due to the fact that each set of equations depicts unique flutter situations with varying speeds and frequencies.

C.2.1 Forced Motion (Elastic Oscillations) (Forcing spring) A linear spring transfers the harmonic motion to the model as shown in Fig.[34]. The derivatives are calculated based on the ratio of amplitude between the force and resonancefrequencies considering phase shift between any two movements.

The equation that governs the movement of the system is given by:

$$I_{zz}\ddot{\theta} + k_\theta\dot{\theta} + \sigma_\theta\theta = C_{m_{\dot{\theta}}}\dot{\theta} + C_{m_\theta}\theta + C_{m_F} \tag{47}$$

where C_{m_F} is the excitation moment coefficient, C_{m_θ} and $C_{m_{\dot{\theta}}}$ are Stiffness and damping derivatives given by:

$$C_{m_\theta} = \sigma_\theta - p^2 I_{zz} - \frac{\overline{C_{m_F}}}{\bar{\theta}}\cos\epsilon \tag{48}$$

$$C_{m_{\dot{\theta}}} = k_\sigma - \frac{\overline{C_{m_F}}}{p\bar{\theta}}\sin\epsilon \tag{49}$$

Where

$$\overline{C_{m_F}} = \text{ Const } \bar{y}_F$$

y_F represents the downward displacement at the point of connection of spring k_1 to the exciter, which is the forcing amplitude. If the structural coefficients of the system (σ_θ, k_θ and I_{zz}) are known, then the derivatives may be calculated in terms of the angular frequency p, amplitude ratio, and phase angle ϵ. The structural coefficients are found by repeating the test in still air, first with the model attached to obtain a value for the model inertia and then without the model attached to obtain a value for k_σ with $C_{m_\theta} = 0$. These tests must be conducted with the exact same amplitude of oscillation $\bar{\theta}$ as the wind-on test. This situation is impossible to achieve without a certain sort of mechanical exciter in which the amplitude may be continually changed during oscillation. The fundamental response equations for this system (spring-tuned system) can be written as:

$$\left(\frac{\bar{\theta}}{\bar{\theta}_a}\right)^2 = \frac{1+4Q^2}{1+4Q^2+4\left(1-\gamma^2\right)^2 Q^2} \tag{50}$$

$$\tan\epsilon = \frac{2\gamma Q}{1+2\left(1-\gamma^2\right)Q^2} \tag{51}$$

Where

$$\gamma = \frac{p}{p_a} \tag{52}$$

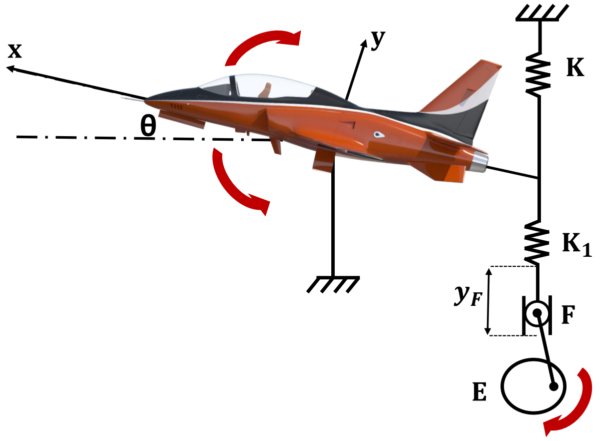

Fig. 34 Elastically forced oscillation

$$Q = \frac{P_a I_{zz}}{k_\theta - C_{m_{\dot{\theta}}}} \tag{53}$$

The suffix a specifies values at amplitude resonance. p, p_a are the angular frequency, amplitude-resonance frequency ,respectively. The sharpness of the tuning is determined by the Q factor. The response curves for these two values of Q computed from eqns. (50), (51). At low speeds, it has a value of 2.5, while at high speeds it may approach 2000. The data demonstrate that near-resonance excitation of a finely tuned system necessitates an extremely stable mechanical oscillator, as slight variations in frequency result in huge changes in amplitude and phase, rendering the calculation of derivatives inaccurate. If the system is stimulated at the amplitude-resonance frequency p_a, the damping formulation is

$$C_{m_{\dot{\theta}}} = k_\theta - \frac{\overline{C_{m_F}}}{p_a \bar{\theta}_a} \frac{1}{\left(1 + \frac{1}{4Q^2}\right)^{1/2}} \tag{54}$$

For realistic values of $Q \geq 2.5$, it is possible to write

$$C_{m_{\dot{\theta}}} = k_\theta - \frac{\overline{C_{m_F}}}{p_a \bar{\theta}_a} \tag{55}$$

The phase angle ϵ is absent, thus its measurement is unnecessary. But the derivative of stuffiness is

$$C_{m_\theta} = \sigma_\theta - p_a^2 I_{zz} \left(1 + \frac{1}{2Q^2}\right) \tag{56}$$

Writing

$$C_{m_\theta} \simeq \sigma_\theta - p_a^2 I_{zz} \tag{57}$$

The equation in R.H.S is proportional to the probability in resonance frequency caused by aerodynamic loading (since $\sigma_\theta \sim p_0^2 I_{zz}$), where suffix "0" specifies circumstances of still air. Low-speed measurements are challenging due to the flat tuning of devices built for such testing. An alternate method is to stimulate at the frequency of resonance. The precise derivatives are then provided by

$$C_{m_\theta} = \sigma_\theta - p_p^2 I_{zz} \tag{58}$$

$$C_{m_{\dot{\theta}}} = k_\theta - \frac{\overline{C_{m_F}}}{p_p \bar{\theta}_p} \tag{59}$$

Where p is a phase resonance condition. A gadget is required to signal when the phase angle $\epsilon = 90^\circ$. Since the phase angle varies quickly with frequency, the resonance frequency can be precisely established.

NASA LaRC conduct a test at 12-Foot Low-Speed Tunnel using the dynamic pitch rig shown in Fig.[35]. The dynamic pitch rig is a computer controlled, hydraulically actuated system that is sting-mounted on a C-strut support

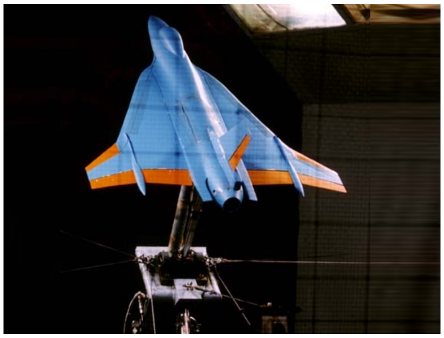

Fig. 35 Dynamic Pitch Motion Test Rig

system, an internally mounted balance is connected in the model. The setup oscillates the model about the moment reference center of the internally mounted balance, this oscillation make the angle of attack range of the model up to 85°.The dynamic test rig has a maximum pitch rate of 260 deg/sec and a pitch acceleration of 2290 deg/sec^2. The dynamic pitch rig can evaluate a wide range of pitching motion. Sinusoidal oscillations of various amplitudes and frequencies, ramp motions (constant pitch rate), sum of sinusoidal motions at various frequencies and amplitudes are examined. Kim and Patrick in [72],[73], the dynamic pitch rig may be further described. Pitch angle data from an LVDT, six component force and moment data from a strain gauge balance, and dynamic pressure of the freestream from a wall-mounted pitot-static probe were all acquired during a test run. With an in-line low-pass anti-aliasing filter, data are typically sampled at 100 Hz. After that, all data channels are digitally filtered, and numerous testing cycles are ensemble averaged to lessen data dispersion.

C.2.2 Forced Motion (Electric Excitation) An electric vibrator replaces the mechanical exciter and spring K_1. The mechanism is depicted in Fig.[36]. The oscillator-powered by a power amplifier supplies the vibrator with current. Through the output control of a valve oscillator, the amplitude may be constantly adjusted in response to electrical stimulation. This simplifies the estimation of structural coefficients dependent on amplitude from static air excitation tests. At high levels of Q associated with high-speed circumstances, the frequency stability and precision of frequency control that may be achieved with valve oscillators provides a further benefit. In the electric self-excitation approach, the amplifier's input signal is collected from a displacement pickup on the oscillating system.The phase shifter modulates the excitation current in quadrature with the displacement, while the amplitude stabilizer maintains the oscillation's fixed amplitude despite variations in wind speed. As the system naturally oscillates at phase response, the approach is advantageous when working with finely-tuned systems operating under high-speed, high-frequency circumstances. When the aerodynamic damping is negative, the vibrator connection should be inverted. In this manner, the excitation sign is inverted, and the driving amplifier functions as a damper. Such a potential cannot be fulfilled by alternative means.

C.2.3 Forced Motion (Excitation with coubled freedom) There are two degrees of freedom in the system. One degree of freedom is used to stimulate the system, and the response near or at each resonance frequency is monitored. The approach presupposes that derivatives do not vary with the frequency parameter, although the assumption of flow and velocity independence does not hold. An implementation of the approach involves oscillating models put on a sting. Due to the flexibility of the sting, an extra edict of freedom is added, and it cannot be suppressed. Considering that the motion of the system is both pitching and diving, with excitation in pitch, eqns.(44)and (45) are applicable, with C_{m_F} added to the right-hand side of eqn. (44)

$$\begin{aligned} C_{m_F} &= \overline{C_{m_F}} e^{jpt} \\ \theta &= \bar{\theta} e^{j(pt-\epsilon_\theta)} \\ y &= \bar{y} e^{j(pt-\epsilon_y)} \end{aligned} \tag{60}$$

Where ϵ_θ and ϵ_y are the phase lag angles by substituting eqn. (60) into eqns. (44) and (45), four equations having eight derivatives are generated. Eight derivatives may be found by evaluating these equations at two resonance frequencies. The excitation may be mechanical or electrical, but the associated motion must be free of flutter in the absence of stimulation.

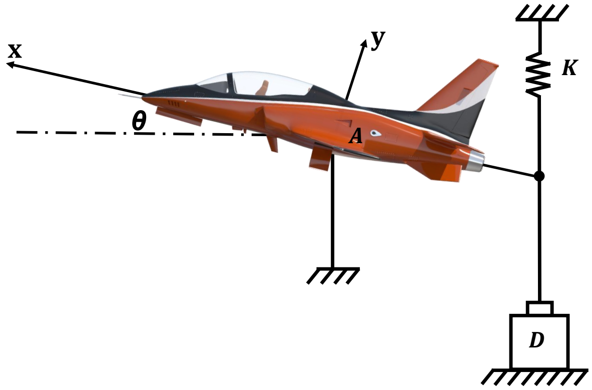

Fig. 36 Electric forced excitation test rig

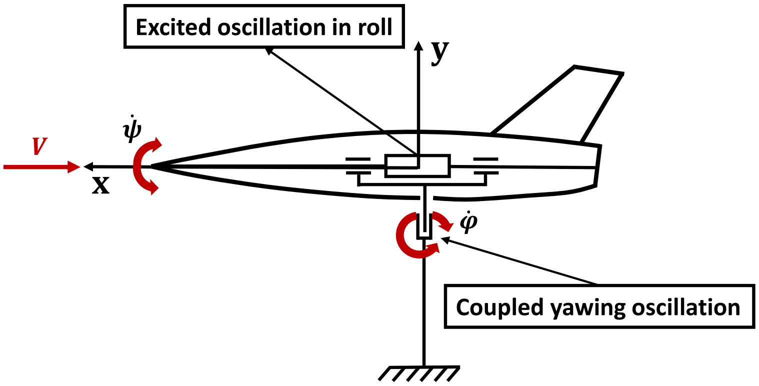

Fig. 37 Cross oscillation excitation test rig

C.2.4 Forced Motion (Cross oscillations) A second application of the method of linked freedom excitation. It is used to calculate the damping cross derivatives C_{l_r} and C_{n_p} as shown in Fig.[37]. In resonance, oscillations are stimulated about one axis. The temporal evolution of coupled motion around the opposite axis and that of the excited axis are recorded. When the derivative C_{n_p} is necessary, for instance, rolling oscillations are excited.

$$I_{yy}\ddot{\psi} + k_{\psi}\dot{\psi} + \sigma_{\psi}\psi - I_{xy}\ddot{\varphi} = C_{n_{\dot{\psi}}}\dot{\psi} + C_{n_{\dot{\varphi}}}\dot{\varphi} + C_{n_{\psi}}\psi + C_{n_{\varphi}}\varphi \tag{61}$$

$$I_{yy}\ddot{\varphi} + \left(k_{\psi} - C_{n_{\dot{\psi}}}\right)\dot{\psi} + \left(\sigma_{\psi} - C_{n_{\psi}}\right)\psi - I_{xy}\ddot{\varphi} = C_{n_{\dot{\psi}}}\dot{\varphi} + C_{n_{\varphi}}\varphi \tag{62}$$

The frequencies of excited and coupled movements are matched, and the phase difference between the two motions is adjusted to be zero. At this time, the aerodynamic and mechanical damping due to yaw work in opposition to the aerodynamic yaw moment owing to roll. Equalizing the left and right quadrature components of the eqns.(61) and (62).

$$\left(k_{\psi} - C_{n_{\dot{\psi}}}\right)\bar{\psi} = C_{n_{\dot{\varphi}}}\bar{\varphi} \tag{63}$$

The amplitudes $\bar{\psi}$ and $\bar{\varphi}$ are derived from the motion record. The direct derivative $C_{n_{\dot{\psi}}}$ is to be found using the aforementioned procedures. The value $C_{n_{\dot{\varphi}}}$ is then obtained, and it immediately equals C_{n_p}.

C.2 Force Measurements During oscillations, the derivatives are calculated based on the forces operating on the model. Force pickups are included into the drive's linkage. The following methods concludes the best rigs used to estimate such derivatives

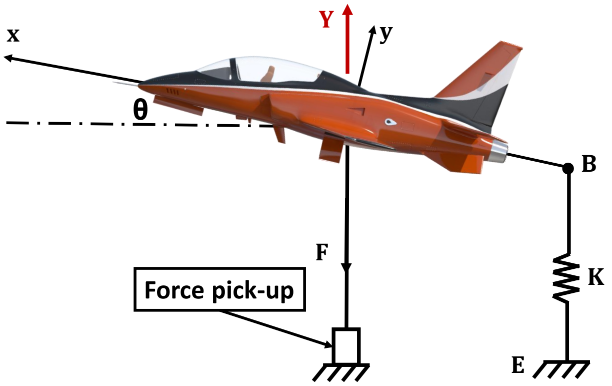

Fig. 38 Free oscillation method with force measuring test rig

C.2.1 Free Oscillations To measure the lift, a force pickup is introduced at the axis of oscillation as shown in fig.[38]. As

$$\theta = \bar{\theta} e^{\mu t} \sin pt$$

As p is the angular frequency. The lift force may be written as:

$$C_L = \overline{C_L} e^{\mu t} \sin(pt + \epsilon) = C_{L_\theta} \theta + C_{L_{\dot{\theta}}} \dot{\theta}$$

The derivatives are then given by:

$$\begin{aligned} \overline{C_L} \cos \epsilon &= \bar{\theta} \left(C_{L_\theta} + \mu C_{L_{\dot{\theta}}} \right) \\ \overline{C_L} \sin \epsilon &= \bar{\theta} p C_{L_\theta} \end{aligned} \tag{64}$$

The value

$$\frac{\overline{C_L}}{\bar{\theta}} = \frac{C_{L_1}}{\theta_1} e^{\mu \epsilon / p}$$

Peak values C_{L_1} and θ_1 are separated by the phase angle ϵ. If the spring K is a torsion spring, the elastic forces in the recorded reaction can be rendered zero. In fig.(40), we see the Bristol one and two DOF pilot rig [74], is suspended head-first from the pendulum strut, providing pitch freedom; the strut's top is positioned on a bearing, providing a "swing" DOF with a dominant component in the heave direction. Using the actuated horizontal tailplanes (stabilators), the model is "flown" in the 3'6" diameter open-jet wind tunnel in these two axes of freedom. Low stresses on the strut minimize sting interference effects, allowing for a pitch angle range of roughly 40 degrees, as well as any arbitrary combination of pitch and heave in concept. The department's 7 ft. by 5 ft. closed-section tunnel can also be outfitted with the equipment for additional testing options. For the purposes of collecting data on unsteady aerodynamics, it is desirable to also measure the aerodynamic reaction, as this reveals information on the delay between the load and the response. The 'binocular' configuration stain gauge balance (to be installed midway along the strut) and the 'ring' balance (almost integral with the model gimbal, therefore allowing it to be situated effectively within the fuselage and out of the flow) are two flexures developed for this purpose. Coupling with the bending loads on the strut has been a primary concern, in addition to the typical difficulties involved with flexure design. The design phase included the use of finite element analysis, and a gauge at the strut's top measures bending stresses for a complete calibration. The first aircraft model built for the 2-DOF system is a 1/16th-scale BAe Hawk with a 600 mm wing span and a weight of approximately 1.2 kg.

Bristol examined a cost-effective three-degree-of-freedom test equipment for determining aircraft static and dynamic stability derivatives [75]. The technique utilized a three-degree-of-freedom gimbaled mechanism to attach a model under active control to a vertical support strut. The support strut was also put on a six-component piezoelectric balance in order to acquire simultaneous aerodynamic force and moment data. With very slight adjustments to the overall configuration, a complete set of static and dynamic stability derivatives was achieved. For the static testing scenario, the

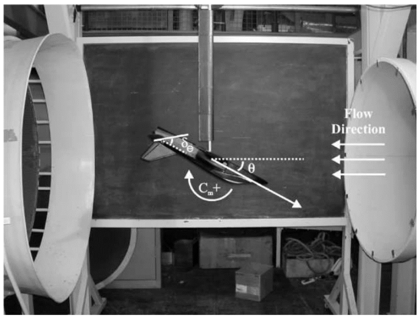

Fig. 39 Hawk model mounted to 2-DOF rig

Fig. 40 1-16th-scale Hawk Model on 2-DOF test rig [74]

model pitch angle was adjusted using a DC shunt motor directly coupled to a vertical leadscrew configuration situated directly behind of faired main strut. This was accomplished by adding an extra pitch arm (not seen in fig.(41) to the model's leadscrew and tail cone. With the M2370 model installed, the pitch range was 15 to 25 degrees, to guarantee the roll and yaw degrees of freedom remained rigid throughout the static testing phase, a specially constructed pitch plate was mounted on top of the gimbal to restrict roll, along with a yaw stopper shown in Fig.[42] that was locked at 0 degrees. To calibrate the static pitch angle, there is a digital inclinometer (with uncertainety up to 1 degree) fixed on the model fuselage and compared to the pitch axis potentiometer reading via the dSpace interface. After calibration, the error in angular position was assessed to be less than 1 degree. The calibration of additional measuring potentiometers for the roll, yaw axes were also found to fall within this error range. For the dynamic testing setup, the pitch arm and pitch plate were eliminated from the system, and the yaw limiter was loosened to enable pitch, roll, and yaw motion without restriction. For all dynamic test setups, the Kistler balance was used to measure the dynamic lift, drag, and side force at the same time as the model moved. Fig.(42) depicts a detailed schematic of the 3-DOF gimbal. The construction of the gimbal included two main frames, one nested within the other, and precise ball bearings that allowed for pitch and roll freedom. A third yaw housing, attached to the inner pitch housing, employed thrust bearings to withstand aerodynamic forces and moments while allowing for unfettered yaw motion. Penny and Giles accurate potentiometers were employed in each of the three axes to measure the pitch, roll, and yaw movements of the model pitch and roll gimbals seen in Fig.(42). The yaw potentiometer was positioned within the yaw enclosure and was directly linked to the mounting axis (not pictured). When performing with 3-DOF capabilities, the pitch, roll, and yaw limitations of the gimbal were 45, 45, and 35 degrees, respectively. A slot in the fuselage was surrounded with semirigid padding to lessen impact stresses on the gimbal bearings in the event that the gimbal limitation was reached. Due to the degree of rotational rotation accomplished with the 3-DOF gimbal, the needed cutout in the fuselage was fairly big, which might have caused a cavity impact on the observed findings. However, no attempt has been made to explain this result. To figure out the stability derivatives, the angular position was numerically differentiated [76] to get the required angular rates and accelerations for the equations of motion.

C.2.2 Forced Oscillations To the model, angular, translational, or combination oscillations are firmly imposed. Measuring the responses between the model and forcing elements. There are no spring components in the system. From the in phase and out of phase components of the observed aerodynamic reaction, the derivatives are derived. This approach can identify all aerodynamic derivatives with the exception of those caused by rotational roll.

C.2.2.1 External rigid drive The model pivots about an axis at A and is powered at B by a stiff link coupled to a mechanical excitation mechanism at E Fig.[43]. Vertical response F_2 at A is measured by a pickup P_2 and the exciting response F_1 is measured by a pickup P_1 in the forcing link. The motion equation around A is [61].

$$I_{zz}\ddot{\theta} + k_{\theta}\dot{\theta} = lF_1 + C_{m_{\dot{\theta}}}\dot{\theta} + C_{m_{\theta}}\theta \tag{65}$$

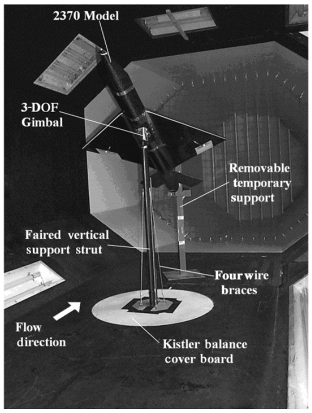
2370 Model
3-DOF Gimbal
Removable temporary support
Faired vertical support strut
Four wire braces
Flow direction
Kistler balance cover board

Fig. 41 The wind tunnel setup for The Bristol 3-DOF dynamic testing

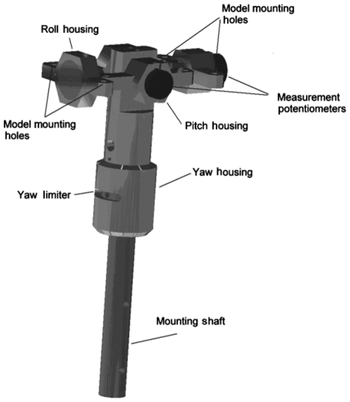

Fig. 42 3-DOF gimbal

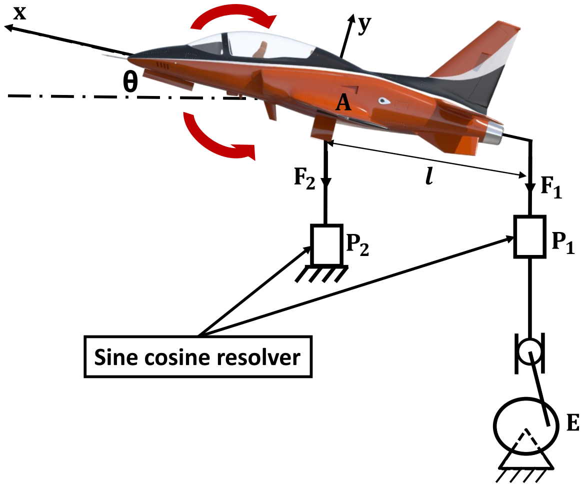

Fig. 43 External rigid drive

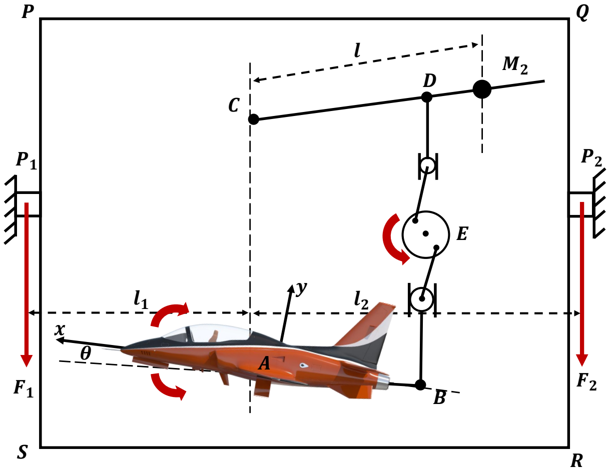

Fig. 44 Internal rigid drive

The structural terms (including inertial responses) in these relationships are established by repeating the test in still air with the same frequency and amplitude as in the test with wind. Frequently, inertial effects are substantial, particularly when the equipment is built for testing at high speeds and frequencies. The aerodynamic forces are then calculated as minor variations between large vector amounts with small phase angles. This results in poor precision. Therefore, inertial forces should be balanced. This frequently poses a substantial number of experimental challenges. The forced movements can be selected so that the model performs a mix of rotational and translational motions while retaining the same orientation with respect to the air stream. From this "snaking motion" it is possible to derive derivatives in pure pitch C_{m_q} or in pure yaw C_{n_r}.

C.2.2.2 Internal rigid drive The configuration guarantees that only aerodynamic loads are detected by the force pickups. On a sturdy floating frame are installed the model, the oscillation mechanism, and the driving motor Fig.(44) It is impossible for the frame to move off of its plane. The motion of the frame in its plane is resisted by force pickups P_1 and P_2 that connect the frame to a rigid earth. These pickups record responses F_1 and F_2 in the frame's plane and perpendicular to the wind's direction. The mass M_1 balances the inertial forces, and the friction forces are contained within the frame.

In a condition of equilibrium

$$\begin{aligned} C_{L_{\dot\theta}}\dot\theta + C_{L_\theta}\theta &= F_1 + F_2 \\ C_{m_{\dot\theta}}\dot\theta + C_{m_\theta}\theta &= F_1 l_1 - F_2 l_2 \end{aligned} \tag{66}$$

The derivatives are given directly by

$$\begin{aligned} C_{L_\theta}\bar\theta &= \bar F_1 \cos\epsilon_1 + \bar F_2 \cos\epsilon_2 \\ C_{L_{\dot\theta}} p\bar\theta &= \bar F_1 \sin\epsilon_1 + \bar F_2 \sin\epsilon_2 \\ C_{m_\theta}\bar\theta &= \bar F_1 l_1 \cos\epsilon_1 - \bar F_2 l_2 \cos\epsilon_2 \\ C_{m_{\dot\theta}} p\bar\theta &= \bar F_1 l_1 \sin\epsilon_1 - \bar F_2 l_2 \sin\epsilon_2 \end{aligned} \tag{67}$$

utilizing preceding section's notations. The enormous frame necessitates force pickups with extremely high stuffiness and hence low sensitivity. This method is appropriate for measuring big forces at low frequencies, such as at high subsonic speeds with a low frequency parameter. Its mechanical design makes it suited for half-model testing with the frame close to and parallel to the wall of the test section, the components on one side and the model on the other side protruding into the wind stream. In the Ankara Wind Tunnel, the dynamic stability derivatives of an oscillating generic combat aircraft model were measured using a direct forced oscillation technique [28]. The model used for the oscillatory tests known as the AGARD, Standard Dynamic Model, and it is produced as a general combat aircraft model to validate different measurement methodologies in several NATO wind tunnels. A five-component internal strain gauge balance installed within the oscillating model is used to quantify aerodynamic forces and moments. Fig.[45] depicts the

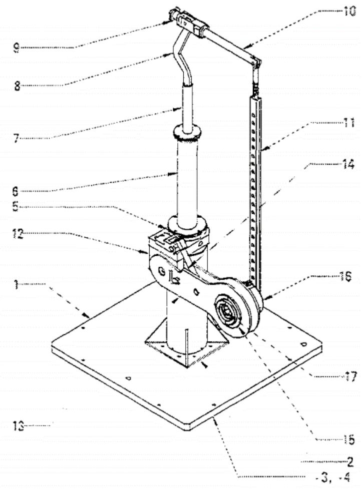

Fig. 45 Parts of the AWT Test Rig

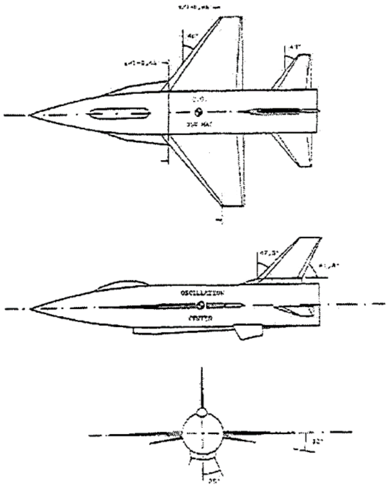

Fig. 46 The geometry of the Standard Dynamic

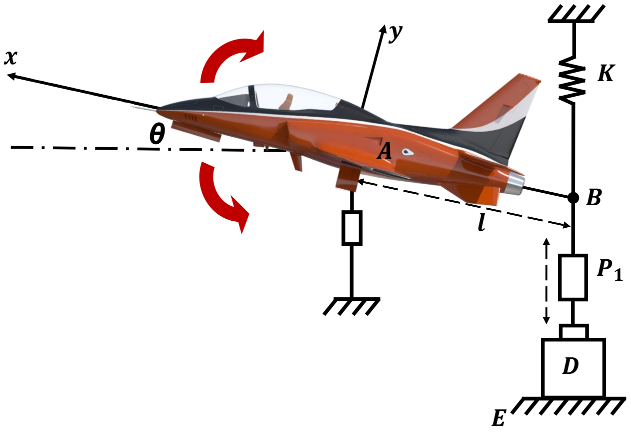

Fig. 47 Electrically excited oscillation for system with force pick-ups

general arrangement of the test rig. The drive mechanism that provides the model's simple harmonic motion in the pitch plane is located beneath the floor of the test section of wind tunnel. The driving unit is powered by a DC-servo motor, that delivers rotational motion to a crank-rod mechanism, which is coupled to an oscillating vertical push rod, which supports the SDM. The amplitude of oscillations for the model is controlled by changing the eccentricity radius of the flywheel, which may be altered within a range of 50 mm, resulting in 5° of pitch oscillations in midel amplitude.

C.2.2.3 Electric Excitation Fig.(47) shows the mechanical exciter E in fig.[43] is replaced by an electric vibrator D that is supplied by a valve oscillator and power amplifier. A spring K is introduced for the purpose of balancing inertial responses. The approach is beneficial due to enhanced control over oscillation frequency and amplitude. This is beneficial for implementing customized processes. For balancing the inertial responses of finely-tuned systems under high-speed test circumstances [61].

C.2.2.4 Fixed Model in Oscillatory Flow Within the test section, an oscillating flow is produced. This can be accomplished, for instance, by a longitudinally oscillating bump on the tunnel wall or a set of oscillating vanes upstream of the model fig.(48). This is the sole way for measuring oscillatory derivatives on models stationary in the test section. However, it is challenging to determine the proper shape of such an oscillating flow.

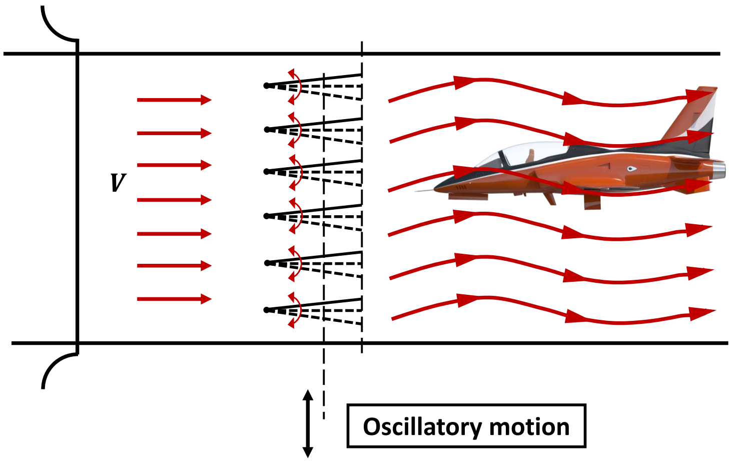

Fig. 48 Test section with oscillatory flow

D. Free Flying Wind Tunnel Tests

The test is conducted in free flight wind tunnels without the use of balances. A model is flown by two or three operators who may adjust wind speed, tunnel axis slope, model engine thrust, and model control position. First, the wind velocity, tunnel slope, and engine thrust are adjusted to maintain balance. Then, model controls are remotely deflected, and the model's reaction is captured by three film cameras in three mutually perpendicular planes. The derivatives are calculated based on the model's transient reaction to control deflection. Typically, longitudinal and lateral derivatives are assessed separately. The model must be dimensionally and dynamically comparable, and its design and fabrication are extremely difficult.

D.1 Free Flying Two of the most challenging aspects of conducting captive-model dynamic-stability tests in wind tunnels are:

- The interference caused by a mechanical model support and its vibration.
- The inadequacy of any mechanical support to simulate the unconstrained model motion.

Consequently, it has been realized that a wind-tunnel approach without the necessity for mechanical model support is necessary for conducting tests by using several techniques as follows:

- Launching model into the wind-tunnel flow and performing free flight in the test section.
- Remotely-controlled models flying in the test section with a flexible control-and-safety cable attached to the model.
- Cable-suspended models, which can perform motion in five degrees of freedom (all but longitudinal translation).
- Magnetically suspended and magnetically actuated models.

The adaption of the free-flight approach to the NAE helium-hypersonic-wind-tunnel. The technology employs a pneumatic launcher and injection-molded polystyrene models. The data is taken from a high-speed film with an average frame rate of (3000–4000 per second). The optical technology allows the model to be seen in two perpendicular planes on the same frame [77]. The pitch-jet launch system allows the model to be launched at a relatively small angle relative to the axis of the launch gun and then to impart an angular velocity to it instantly after release; the maximum (large) angle of attack will then be achieved only when the model reaches the observation area, without significantly altering its trajectory. The model may be spun up on a spindle prior to release, and one or two air jets installed on the launch head impart the angular velocity after launch. An alternate shot-put launch utilizes a rail-type support in place of the spindle, with one missile fin guided in a slot along the rail, whose angle may be adjusted between 0 and 90 degrees. A complete explanation of the procedural particulars pertaining to strategies employing free flight in wind tunnels found in [77–80]. The NASA-Langley-Full-Scale-Wind-Tunnel provides a unique testing capability for flight. This tunnel's 30 ft x 60 ft open test section allows for the unrestricted flight of reasonably large (usually approximately 4 ft span) powered models [81]. Three operators are able to deliver electric and pneumatic power and command signals to the model through a flexible cable. This flexible cable also includes a small steel safety line that passes through a pulley above the test section and can be utilized to grab the model in the event of an uncontrollable motion or mechanical breakdown. During

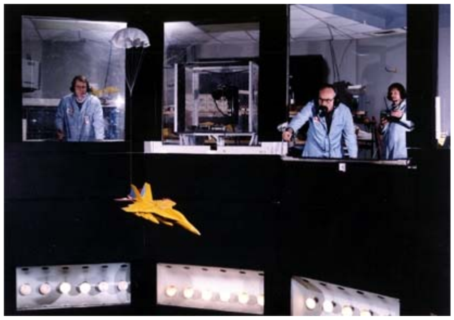

Fig. 49 Free-spin test of dynamically-scaled fighter model

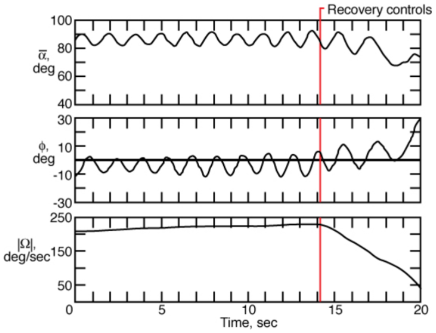

Fig. 50 Typical spin time history in VST

flight, the whole flight cable is maintained loose and is handled by a secondary safety-cable operator. Examples of typical outcomes include stable flights at high angles of attack, investigations of pilot control techniques at high angles of attack, and evaluations of artificial rate dampening. Most of the results are qualitative and come from pilot tests of how the model behaves and film documentation.

D.2 Free Spin One of the most prevalent applications of dynamically scaled models in the Vertical Spin Tunnel (VST) is the detection and analysis of airplane spin modes and spin-recovery characteristics, including size requirements for emergency spin recovery parachutes as shown in fig.(49). Spin models are manually launched with pre-rotation at a steep attack angle into a vertically ascending air stream. The tunnel operator modifies the test section's velocity to satisfy the model's sink rate. If one or more spin modes exist, the model's attitude and spin rate will tend to stabilize (or oscillate about mean values). Fig.[50] is an example of a time history from a free-spin test, where the pitch angle, roll angle, and spin rate of a model are shown versus time. The shown spin is "fixed" yet oscillatory, meaning that the pitch and roll angles fluctuate about a mean value. Notably, the spin rate could not stabilize until roughly 10 seconds into the experiment. At about 13.2 seconds into this test, the recovery control command was launched by sending a signal from the radio transmitter to the model's on-board receiver, which directed servos to drive the control surfaces to their pre-determined recovery deflections , resulting in the spin rate starting to bleed off and the pitch and roll angles dramatically diverging from those during the "steady" spin.

D.3 Free Tumble Similar to free-spin testing, flying-wing and other non-conventional designs are subjected to tumble tests [82]. Due to the fact that a tumbling model generates net lift and hence lacks a vertical flight path as a spinning model, testing is often brief as the model passes the test area. A "free-to-pitch" rig is utilized when longer test times are necessary. This setup only lets the model spin around the pitch axis (1-DOF), but tests of any length can be done.

E. Flight Testing

Flight testing in aeronautical engineering involves the systematic acquisition of aircraft performance data during its operational flight. Subsequently, these collected data are subjected to rigorous analysis to derive crucial aerodynamic characteristics and assess system integrity. The primary objective of flight-testing Unmanned Aerial Vehicles (UAVs) is to ascertain the aircraft's capability to safely accomplish its designated mission. Additional objectives encompass the collection of data pertaining to aerodynamics, propulsion systems, and various onboard systems, as well as the pursuit of research in these areas and other pertinent fields [**?**].

Traditionally, there exist four fundamental categories of flight testing. The first category encompasses experimental endeavors driven by the pursuit of expanding our knowledge and pushing the boundaries of aeronautics. Such testing has its historical roots in seminal moments such as the Wright Brothers' pioneering flights [83] and subsequent X-series research endeavors during the mid-20th century[84] . The second category focuses on the development of commercial aircraft products. Aircraft manufacturers continuously strive to innovate and enhance their products to remain competitive in the aviation industry. Consequently, these new aircraft designs undergo rigorous testing to characterize their performance and identify operational challenges [85]. The third category involves evaluating whether newly designed aircraft can effectively accomplish their intended missions. This assessment ensures that the aircraft meet the operational requirements and objectives set during their design phase. The fourth and final category of flight testing pertains to compliance with established aviation safety regulations and standards. Government agencies play a specialized role in conducting these regulatory tests, and compliance is an essential prerequisite for the commercial sale of aircraft. The flight test phase is inherently non-profitable and carries an elevated risk profile due to potential accidents or hazardous events. This increased risk is often attributed to the absence of comprehensive data integration in the aircraft design process, the lack of established operational procedures, and the potential inadequacy of test pilot training or flight crew experience. Consequently, the process of flight testing is structured into three distinct stages: planning, execution, and data analysis and reporting. The success or failure of a flight test program hinges on the effectiveness of the planning stage, which enables the flight test crew to devise the most efficient and safe approach to execute the program. During this stage, the flight test objectives are defined, and the crew determines the most suitable test types and techniques to achieve these objectives. Experiments are then grouped to minimize the total number of required flights, and appropriate sensors are selected to fulfill the testing objectives. The final stage involves data extraction from onboard instruments and comprehensive data analysis and reporting.

Previous works by Liu [86], [87] have delved into the design and planning of flight tests for manned aircraft, covering aspects such as the measurement of atmospheric parameters, level flight performance, airspeed calibration, climbs, takeoffs, landings, stick-fixed neutral points, and phugoid mode. Dantsker [88] has proposed an autonomous process for flight testing, aimed at streamlining the determination of flight dynamics parameters. This autonomous process encompasses the measurement of trim, stall speed, stall polar, phugoid mode, idle descent, doublets, and singlets.

The objective of our study is to apply the established scientific principles of flight testing outlined in reference [89] to a small unmanned aerial vehicle. Specifically, we aim to evaluate the takeoff speed, stall speed, and climb performance of the UAV. The subsequent sections of this paper present a comprehensive description of the case study UAV, flight test hypotheses, data predictions, the experimental test matrix for flight testing, the analysis of flight test data, and ultimately, our conclusions regarding the flight test process employed.

E.1 Model Drop Test The helicopter drop-model approach entails dropping a dynamically scaled, unpowered model from a height as shown in fig.(51), flying it through a sequence of maneuvers by remote control at the ground, and retrieving it using a flight termination parachute. To satisfy dynamic scaling requirements, common helicopter drop models are typically quarter-scale and weigh between 500 and 1200 pounds. The model is dropped from up to 15,000 feet and monitored by a manually operated ground-based tracker equipped with video cameras, a radar range system, and telemetry antennae. The comparable aircraft altitude depends solely on the model's scale factor, model mass ratio, and air density; for the F/A-18E/F, a model altitude of 15,000 feet corresponds to around 35,000 feet at full size. A camera is fitted in the model's canopy to offer a pilot's perspective. The pilot rests at a control station and watches data displays and video views while giving three-axis control through a customized cockpit, as seen in Fig.[52]. The global control loop is comprised of down-linked flight data, a computer on which the control rules are implemented, and an uplink command. Once the pilot has executed the intended profile, the onboard flight termination parachute is deployed to decelerate the model for landing. The drop model carries an extensive complement of flight instrumentation to provide real-time state feedback information to the flight control computer, to drive real-time data displays for the ground-based pilot, and for postflight data analysis. Duplex flight sensors measure angle of attack, sideslip, airspeed, 3-axis angular rates and linear accelerations, and 3-axis attitude. Simplex flight instruments include pitot and static pressures, radar range, pilot's-eye-view video, and control surface position transducers. Various system-monitoring parameters and all of the flight sensor signals are down-linked to a ground-based data logging system and, along with pilot comments, video imagery from the ground, and digital recordings of ground-generated signals (such as pilot commands and mode selections) form the collection of data obtained during a flight.

E.2 Flight Model One contemporary UAV project uses a foam airframe paired with a hobby-style motor to do research on sophisticated controls [90]. This project employs as much commercially available and amateur equipment as feasible. This project has performed hundreds of flight tests in only a few years due to the relative simplicity and affordability of its components. Several UAV projects being done by numerous small organizations and colleges are indicative of the low-cost and high-quality nature of the study. These projects often utilize non-dynamically scaled test items and must be mindful of the restrictions that this presents. For instance, the low mass moment of inertia commonly associated with non-dynamically scaled vehicles results in increased maneuvering performance that is not typical of the vehicle being represented; nonetheless, the non-dynamically scaled model can provide insight into trimmed flying performance. Another contemporary UAV project [91] employs a jet-powered, dynamically scaled, custom-built model with custom-designed instruments. Due to the high expenses involved with this concept, a pilot training programme has been implemented to decrease operational risks. Ground support and flight operations need a team of highly seasoned

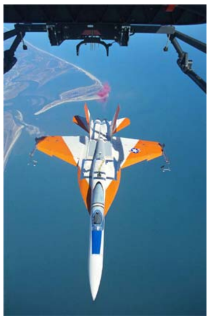

Fig. 51 Drop model just released from helicopter

Fig. 52 Drop model cockpit

experts. This project features a ground station similar to the drop-model depicted above that acts as both the flight station and a flight-team training facility to provide direct experience with day-of-flight human interfaces. New electronic sensors and control technologies make economical, high-quality flight research with subscale models possible and have spawned an abundance of tiny UAV projects around the country.

VII. Conclusion

The review of techniques for evaluating aerodynamic derivatives has highlighted the importance of each method and its suitability for specific stages in the design process. Analytical methods are highly accurate and efficient, making them useful for initial design and concept evaluation. However, they are limited to simple geometries and require significant expertise. Empirical methods, on the other hand, are useful for complex geometries and can be easily applied, but are limited by the availability of experimental data. These methods involve testing physical models in wind tunnels or flight tests to measure the forces and moments acting on the model. Empirical methods provide accurate and reliable data that can be used to validate and verify the results of analytical, numerical, and other methods. Numerical methods have been developed to handle complex geometries and are highly versatile, making them useful for detailed design and optimization. These methods are based on mathematical models that simulate the behavior of the system being analyzed. Numerical methods can provide accurate and detailed information about the aerodynamic derivatives of a system, which is essential for designing and optimizing aerospace vehicles. However, numerical methods require significant computational resources, including high-performance computing and advanced software tools. The accuracy of numerical methods can also be sensitive to modeling assumptions, which can lead to errors and inaccuracies in the results. Therefore, it is important to carefully validate and verify the results of numerical methods using experimental data. Experimental methods remain the most effective and precise technique for obtaining aeromechanical derivatives. However, they are also the most difficult and costly technique for obtaining aerodynamic derivatives. They require specialized facilities, equipment, and personnel, which can be expensive and time-consuming. Therefore, it is important to carefully plan and execute experimental tests to ensure that the data obtained is accurate and reliable. Table.3 shows how different experimental techniques can measure aerodynamic derivatives. This table acts as a visual guide, making it easier for readers to understand how these methods work. Whether you're an expert in the field or new to it, fig.(53) illustrates the effectiveness and importance of these experimental techniques in assessing aerodynamic derivatives, specifically focusing on power and weight considerations. These illustrations can help you see how these techniques are used to measure important aerodynamic data. We've included it to make our research more accessible and to enhance everyone's understanding of aerodynamics in aeronautical science.

In conclusion, a comprehensive understanding of aerodynamic derivatives requires a combination of analytical, empirical, numerical, and experimental methods. Each method plays a crucial role in the design process, and no method cancels the importance of the other. The review presented in this paper provides a valuable resource for researchers, engineers, and aviation enthusiasts seeking to gain a deeper understanding of aerodynamic derivatives and their applications. The insights and comprehensive coverage presented in this review make it a valuable addition to the literature on aerodynamics.

	Static		Continuous				Oscillatory Deflection										
							Measurement of Motion						Measurement of Force				
	Similar Model	Distort Model	Rolling Model	Whirling Arm	Curved Flow	Rolling Flow	Free Oscillations	Flutter Oscillations	Elastic Oscillations	Electric Oscillations	Excitation with coupled freedom	Cross Oscillations	Free Oscillations	External Rigidly Drive	Internal Rigidly Drive	Electric Excitation	Fixed Model in Oscillatory Flow
C_{l_β}	✓						✓	✓	✓	✓	✓		✓	✓	✓	✓	✓
C_{l_p} $(Osc.)$							✓	✓	✓	✓	✓		✓	✓	✓	✓	✓
$C_{l_p}(Rot.)$		✓	✓			✓											
C_{l_r}		✓		✓	✓									✓	✓	✓	
$C_{l_{\dot{\beta}}}$														✓	✓	✓	
$C_{l_r} - C_{l_{\dot{\beta}}}$														✓	✓	✓	
C_{n_β}	✓						✓	✓	✓	✓	✓		✓	✓	✓	✓	✓
$C_{n_p}(Osc.)$																	
$C_{n_p}(Rot.)$		✓	✓			✓						✓					
C_{n_r}		✓		✓	✓									✓	✓	✓	
$C_{n_{\dot{\beta}}}$														✓	✓	✓	
$C_{n_r} - C_{n_{\dot{\beta}}}$							✓	✓	✓	✓	✓		✓	✓	✓	✓	✓
C_{m_α}	✓						✓	✓	✓	✓	✓		✓	✓	✓	✓	✓
C_{m_q}		✓		✓	✓									✓	✓	✓	
$C_{m_{\dot{\alpha}}}$														✓	✓	✓	
$C_{m_q} + C_{m_{\dot{\alpha}}}$							✓	✓	✓	✓	✓		✓	✓	✓	✓	✓
C_{L_α}	✓						✓	✓	✓	✓	✓		✓	✓	✓	✓	✓
C_{L_q}		✓		✓	✓									✓	✓	✓	
$C_{L_{\dot{\alpha}}}$														✓	✓	✓	
$C_{L_q} - C_{L_{\dot{\alpha}}}$							✓	✓	✓	✓	✓		✓	✓	✓	✓	✓
C_{Y_β}	✓						✓	✓	✓	✓	✓		✓	✓	✓	✓	✓
C_{Y_p} $(Osc.)$														✓	✓	✓	
C_{Y_p} $(Rot.)$		✓	✓			✓						✓					
C_{Y_r}		✓		✓	✓									✓	✓	✓	
$C_{Y_{\dot{\beta}}}$														✓	✓	✓	
$C_{Y_r} - C_{Y_{\dot{\beta}}}$							✓	✓	✓	✓	✓		✓	✓	✓	✓	✓

Table 3 Conclusion of experimental techniques abilities

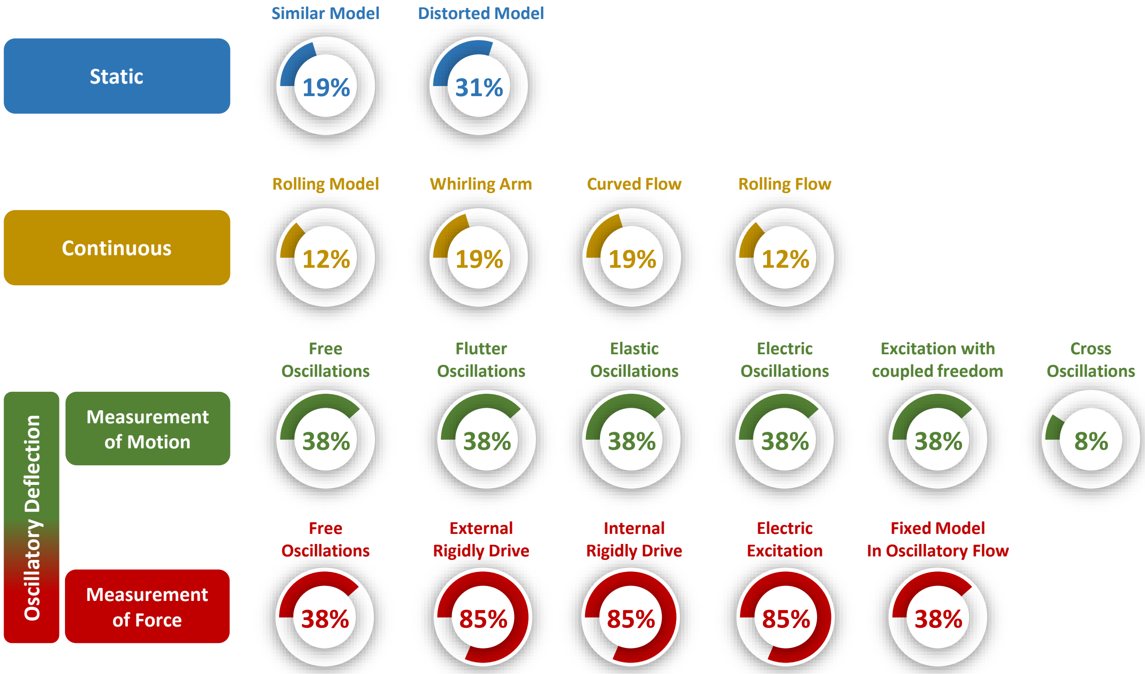

Fig. 53 Illustration of the weight of every experimental technique

References

[1] Orlik-Ruckemann, K., "Review of techniques for determination of dynamic stability parameters in wind tunnels," *AGARD Lecture Series*, , No. 114, 1981.

[2] Babister, A. W., *Aircraft Dynamic Stability and Response: Pergamon International Library of Science, Technology, Engineering and Social Studies*, Elsevier, 2013.

[3] Theodorsen, T., Garrick, I. E., and for Aeronautics, U. S. N. A. C., *General potential theory of arbitrary wing sections*, US Government Printing Office New York, 1933.

[4] Theodorsen, T., "General theory of aerodynamic instability and the mechanism of flutter," Tech. rep., 1949.

[5] Etkin, B., and Reid, L. D., *Dynamics of flight: stability and control*, John Wiley & Sons, 1995.

[6] Williams, J. E., and Vukelich, S. R., "The USAF stability and control digital dATCOM. Volume I. Users manual," Tech. rep., MCDONNELL DOUGLAS ASTRONAUTICS CO ST LOUIS MO, 1979.

[7] Mattsaits, G., "An update of the digital Datcom computer code for estimating dynamic stability derivatives," Tech. rep., AEDC-TR-81-30, 1982.

[8] Blake, W., "Prediction of fighter aircraft dynamic derivatives using Digital Datcom," *3rd Applied Aerodynamics Conference*, 1985, p. 4070.

[9] Jaslow, H., "Aerodynamic relationships inherent in Newtonian impact theory." *AIAA Journal*, Vol. 6, No. 4, 1968, pp. 608–612.

[10] Tobak, M., and Wehrend, W. R., "Stability derivatives of cones at supersonic speeds," Tech. rep., 1956.

[11] Hui, W., and Tobak, M., "Unsteady Newton-Busemann flow theory. Part 2: bodies of revolution," Tech. rep., 1981.

[12] Ericsson, L. E., "Unsteady aerodynamics of an ablating flared body of revolution including effect of entropy gradient." *AIAA Journal*, Vol. 6, No. 12, 1968, pp. 2395–2401.

[13] Ericsson, L.-E., "Unsteady embedded Newtonian flow(as basis for nose bluntness effect on aerodynamics of hypersonic slender bodies)," *Astronautica Acta*, Vol. 18, 1973, pp. 309–330.

[14] Ashley, H., and Zartarian, G., "Piston theory-a new aerodynamic tool for the aeroelastician," *Journal of the Aeronautical Sciences*, Vol. 23, No. 12, 1956, pp. 1109–1118.

[15] Chen, J., "Pitching derivatives of wing in supersonic and hypersonic stream—method for local flow piston theory," *Acta Aerodyn Sin*, Vol. 9, No. 4, 1991, pp. 469–476.

[16] Zhang, W.-W., Ye, Z.-Y., Zhang, C.-A., and Liu, F., "Supersonic flutter analysis based on a local piston theory," *AIAA Journal*, Vol. 47, No. 10, 2009, pp. 2321–2328.

[17] Ye, C., and Dongli, M., "An aircraft steady dynamic derivatives calculation method," *2012 Proceedings of International Conference on Modelling, Identification and Control*, IEEE, 2012, pp. 855–860.

[18] DeSpirito, J., Silton, S. I., and Weinacht, P., "Navier-Stokes predictions of dynamic stability derivatives: evaluation of steady-state methods," *Journal of Spacecraft and Rockets*, Vol. 46, No. 6, 2009, pp. 1142–1154.

[19] Park, M., and Green, L., "Steady-state computation of constant rotational rate dynamic stability derivatives," *18th applied aerodynamics conference*, 2000, p. 4321.

[20] Guglieri, G., and Quagliotti, F., "Dynamic stability derivatives evaluation in a low-speed wind tunnel," *Journal of aircraft*, Vol. 30, No. 3, 1993, pp. 421–423.

[21] Hanff, E., and Orlik-Ruckemann, K., "Wind-tunnel measurement of dynamic cross-coupling derivatives," *Journal of Aircraft*, Vol. 15, No. 1, 1978, pp. 40–46.

[22] Baigang, M., Hao, Z., and Ban, W., "Computational Investigation of simulation on the dynamic derivatives of flight vehicle," *29th Congress of the International Council of the Aeronautical Sciences*, ICAS St. Petersburg, Russia, 2014, pp. 1–7.

[23] Liu, X., Liu, W., and Zhao, Y., "Navier–Stokes predictions of dynamic stability derivatives for air-breathing hypersonic vehicle," *Acta Astronautica*, Vol. 118, 2016, pp. 262–285.

[24] Moelyadi, M., and Sachs, G., "CFD based determination of dynamic stability derivatives in yaw for a bird," *Journal of Bionic Engineering*, Vol. 4, No. 4, 2007, pp. 201–208.

[25] Hui, W. H., "Stability of oscillating wedges and caret wings in hypersonic and supersonic flows." *AIAA Journal*, Vol. 7, No. 8, 1969, pp. 1524–1530.

[26] Le Roy, J. F., and Morgand, S., "SACCON CFD static and dynamic derivatives using elsA," *28th AIAA applied aerodynamics conference*, 2010, p. 4562.

[27] Le Roy, J.-F., Morgand, S., and Farcy, D., "Static and dynamic derivatives on generic UCAV without and with leading edge control," *32nd AIAA applied aerodynamics conference*, 2014, p. 2391.

[28] Alemdaroglu, N., Iyigun, I., Altun, M., Uysal, H., Quagliotti, F., and Guglieri, G., "Determination of dynamic stability derivatives using forced oscillation technique," *40th AIAA Aerospace Sciences Meeting & Exhibit*, 2002, p. 528.

[29] Ronch, A. D., Vallespin, D., Ghoreyshi, M., and Badcock, K., "Evaluation of dynamic derivatives using computational fluid dynamics," *AIAA journal*, Vol. 50, No. 2, 2012, pp. 470–484.

[30] Moore, F. G., and Swanson Jr, R. C., "Dynamic derivatives for missile configurations to Mach number three," *Journal of Spacecraft and Rockets*, Vol. 15, No. 2, 1978, pp. 65–66.

[31] Sahu, J., "Numerical computations of dynamic derivatives of a finned projectile using a time-accurate CFD method," *AIAA Atmospheric Flight Mechanics Conference and Exhibit*, 2007, p. 6581.

[32] Bhagwandin, V., "Numerical prediction of roll damping and Magnus dynamic derivatives for finned projectiles at angle of attack," *30th AIAA applied aerodynamics conference*, 2012, p. 2905.

[33] Oktay, E., and Akay, H., "CFD predictions of dynamic derivatives for missiles," *40th AIAA aerospace sciences meeting & exhibit*, 2002, p. 276.

[34] Mialon, B., Khrabov, A., Da Ronch, A., Cavagna, L., Zhang, M., and Ricci, S., "Benchmarking the prediction of dynamic derivatives: Wind tunnel tests, validation, acceleration methods," *AIAA atmospheric flight mechanics conference*, 2010, p. 8244.

[35] Mialon, B., Khrabrov, A., Khelil, S. B., Huebner, A., Da Ronch, A., Badcock, K., Cavagna, L., Eliasson, P., Zhang, M., Ricci, S., et al., "Validation of numerical prediction of dynamic derivatives: The DLR-F12 and the Transcruiser test cases," *Progress in Aerospace Sciences*, Vol. 47, No. 8, 2011, pp. 674–694.

[36] Forsythe, J. R., Fremaux, C. M., and Hall, R. M., "Calculation of static and dynamic stability derivatives of the F/A-18E in abrupt wing stall using RANS and DES," *Computational fluid dynamics 2004*, Springer, 2006, pp. 537–542.

[37] Green, L., Spence, A., and Murphy, P., "Computational methods for dynamic stability and control derivatives," *42nd AIAA Aerospace Sciences Meeting and Exhibit*, 2004, p. 15.

[38] Mi, B., Zhan, H., and Chen, B., "Calculating dynamic derivatives of flight vehicle with new engineering strategies," *International Journal of Aeronautical and Space Sciences*, Vol. 18, No. 2, 2017, pp. 175–185.

[39] Ghoreyshi, M., Lofthouse, A. J., Findlay, D. B., and Lee, J., "Indicial methods for the numerical calculation of dynamic derivatives," *AIAA Journal*, Vol. 55, No. 7, 2017, pp. 2279–2294.

[40] Mi, B.-g., Zhan, H., and Chen, B.-b., "New systematic CFD methods to calculate static and single dynamic stability derivatives of aircraft," *Mathematical Problems in Engineering*, Vol. 2017, 2017.

[41] Stetson, K., and Sawyer, F., "A comparison of hypersonic wind tunnel data obtained by static and free oscillation testing techniques," *10th Fluid and Plasmadynamics Conference*, 1977, p. 690.

[42] Liu, X., Liu, W., and Zhao, Y., "Unsteady vibration aerodynamic modeling and evaluation of dynamic derivatives using computational fluid dynamics," *Mathematical Problems in Engineering*, Vol. 2015, 2015.

[43] Tuling, S., "Modelling of dynamic stability derivatives using CFD," *25th International Congress of the Aeronautical Sciences, Hamburg, Germany*, 2006, pp. 1–9.

[44] Dufour, G., Sicot, F., Puigt, G., Liauzun, C., and Dugeai, A., "Contrasting the harmonic balance and linearized methods for oscillating-flap simulations," *AIAA journal*, Vol. 48, No. 4, 2010, pp. 788–797.

[45] Ekici, K., Hall, K. C., and Dowell, E. H., "Computationally fast harmonic balance methods for unsteady aerodynamic predictions of helicopter rotors," *Journal of Computational Physics*, Vol. 227, No. 12, 2008, pp. 6206–6225.

[46] McMullen, M., Jameson, A., and Alonso, J., "Demonstration of nonlinear frequency domain methods," *AIAA journal*, Vol. 44, No. 7, 2006, pp. 1428–1435.

[47] Thomas, J. P., Dowell, E. H., and Hall, K. C., "Nonlinear inviscid aerodynamic effects on transonic divergence, flutter, and limit-cycle oscillations," *AIAA journal*, Vol. 40, No. 4, 2002, pp. 638–646.

[48] Hall, K. C., Ekici, K., Thomas, J. P., and Dowell, E. H., "Harmonic balance methods applied to computational fluid dynamics problems," *International Journal of Computational Fluid Dynamics*, Vol. 27, No. 2, 2013, pp. 52–67.

[49] Mader, C. A., and Martins, J. R., "Derivatives for time-spectral computational fluid dynamics using an automatic differentiation adjoint," *AIAA journal*, Vol. 50, No. 12, 2012, pp. 2809–2819.

[50] Lijun, X., Yunjun, Y., Zhou, L., and Weijiang, Z., "High-performance computing of periodic unsteady flow based on time spectral method," *Procedia Engineering*, Vol. 99, 2015, pp. 1526–1530.

[51] Bird, J. D., Cowan, J. W., and Jaquet, B. M., "Effect of fuselage and tail surfaces on low-speed yawing characteristics of a swept-wing model as determined in curved-flow test section of Langley stability tunnel," Tech. rep., 1948.

[52] Lutze, F., "Experimental determination of pure rotary stability derivatives using curved and rolling flow wind tunnel," *18th Aerospace Sciences Meeting*, 1980, p. 309.

[53] Gainer, T., Henderson, W., and Phillips, W., "Rolling stability derivatives of a variable-sweep tactical fighter model at subsonic and transonic speeds," Tech. rep., 1967.

[54] Avcı, S., "Static and forced oscillatory tests on a generetic combat aircraft model in Ankara wind tunnel," Master's thesis, Middle East Technical University, 2000.

[55] Şahin, T., "Modification of the oscillating test rig in Ankara wind tunnel for roll oscillations and measurement of dynamic stability derivatives," Master's thesis, Middle East Technical University, 2001.

[56] Tobak, M., and Schiff, L. B., "Generalized formulation of nonlinear pitch-yaw-roll coupling: Part I-nonaxisymmetric bodies," *AIAA Journal*, Vol. 13, No. 3, 1975, pp. 323–326.

[57] Chambers, J. R., Bowman Jr, J. S., and Malcolm, G. N., "Stall/spin test techniques used by NASA," *AGARD Flight Mechanics Panel Specialists' Meeting on Stall/Spin Problems of Military Aircraft, Brussels, Belgium*, 1975.

[58] Bihrle Jr, W., Hultberg, R., and Mulcay, W., "Rotary balance data for a typical single-engine low-wing general aviation design for an angle-of-attack range of 30 deg to 90 deg," Tech. rep., 1978.

[59] Malcolm, G., and Davis, S., "New NASA-Ames wind-tunnel techniques for studying airplane spin and two-dimensional unsteady aerodynamics," *AGARD Dyn. Stability Parameters*, 1978.

[60] Denham, C. L., and Owens, D. B., "Rotary balance wind tunnel testing for the FASER flight research aircraft," *AIAA Atmospheric Flight Mechanics Conference*, 2016, p. 3105.

[61] Bratt, J., "Wind-tunnel techniques for the measurement of oscillatory derivatives," 1960.

[62] Davison, P., Lowenberg, M., and di Bernardo, M., "Modelling non-linear behaviour in a single degree-of-freedom dynamic wind tunnel rig," *AIAA atmospheric flight mechanics conference and exhibit*, 2003, p. 5314.

[63] Trieu, B., Tyler, T., Stewart, B., Chamock, J., Fisher, D., Heim, E., Brandon, J., and Grafton, S., "Development of a forced oscillation system for measuring dynamic derivatives of fluidic vehicles," *38th Aerospace mechanisms symposium*, 2006.

[64] Cook, M., "On the use of small scale aircraft models for dynamic wind tunnel investigation of stability and control," *Transactions of the Institute of Measurement and Control*, Vol. 9, No. 4, 1987, pp. 190–197.

[65] Carnduff, S., Erbsloeh, S., Cooke, A., and Cook, M., "Characterizing stability and control of subscale aircraft from wind-tunnel dynamic motion," *Journal of aircraft*, Vol. 46, No. 1, 2009, pp. 137–147.

[66] Pattinson, J., Lowenberg, M., and Goman, M., "A multi-degree-of-freedom rig for the wind tunnel determination of dynamic data," *AIAA Atmospheric Flight Mechanics Conference*, 2009, p. 5727.

[67] Navaratna, P. D. B., "Virtual Flight Testing in a Wind Tunnel Using a Manoeuvre Rig," Ph.D. thesis, University of Bristol, 2020.

[68] Pattinson, J., "Development and evaluation of a wind tunnel manoeuvre rig," Ph.D. thesis, University of Bristol, 2010.

[69] Peyada, N., Ghosh, A., and Go, T., "Mathematical modelling, simulation, and estimation of aircraft parameters using five degree-of-freedom dynamic test rig," *Proceedings of the Institution of Mechanical Engineers, Part G: Journal of Aerospace Engineering*, Vol. 226, No. 1, 2012, pp. 55–63.

[70] Pattinson, J., Lowenberg, M. H., and Goman, M., "Multi-degree-of-freedom wind-tunnel maneuver rig for dynamic simulation and aerodynamic model identification," *Journal of Aircraft*, Vol. 50, No. 2, 2013, pp. 551–566.

[71] Araujo-Estrada, S. A., Gong, Z., Lowenberg, M. H., Neild, S., and Goman, M., "Wind tunnel manoeuvre rig: a multi-DOF test platform for model aircraft," *54th AIAA Aerospace Sciences Meeting*, 2016, p. 2119.

[72] Kim, S., Murphy, P., and Klein, V., "Evaluation and Analysis of F-16XL Wind Tunnel Data from Dynamic Tests," *AIAA Atmospheric Flight Mechanics Conference and Exhibit*, 2003, p. 5396.

[73] Murphy, P., and Klein, V., "Validation of methodology for estimating aircraft unsteady aerodynamic parameters from dynamic wind tunnel tests," *AIAA Atmospheric Flight Mechanics Conference and Exhibit*, 2003, p. 5397.

[74] Lowenberg, M., and Kyle, H., "Development of a pendulum support rig dynamic wind tunnel apparatus," *AIAA atmospheric flight mechanics conference and exhibit*, 2002, p. 4879.

[75] Gatto, A., and Lowenberg, M., "Evaluation of a three degree of freedom test rig for stability derivative estimation," *Journal of Aircraft*, Vol. 43, No. 6, 2006, pp. 1747–1761.

[76] Rajamurthy, M., "Generation of comprehensive longitudinal aerodynamic data using dynamic wind-tunnel simulation," *Journal of Aircraft*, Vol. 34, No. 1, 1997, pp. 29–33.

[77] ŁUCJANEK, W., and ADAMS, P., "Development of free-flight technique for NAE helium hypersonic wind tunnel," *DME/NAE Quarterly Bulletin*, Vol. 3, 1966, pp. 61–104.

[78] Beyers, M. E., "ANALYSIS OF HIGH-MANOEUVRABILITY VEHICLES IN FREE FLIGHT." 1980.

[79] Beyers, M., "Investigation of High Manoeuvrability Flight Vehicle Dynamics," *ICAS Proceedings*, Vol. 80, 1980, pp. 278–292.

[80] Dayman Jr, B., "Free-flight testing in high-speed wind tunnels," Tech. rep., 1966.

[81] Grafton, S. B., Chambers, J. R., and Coe Jr, P. L., "Wind-tunnel free-flight investigation of a model of a spin-resistant fighter configuration," Tech. rep., 1974.

[82] Fremaux, C., Vairo, D., and Whipple, R., "Effect of geometry and mass distribution on tumbling characteristics of flying wings," *Journal of aircraft*, Vol. 32, No. 2, 1995, pp. 404–410.

[83] Jakab, P. L., *Visions of a flying machine: The Wright brothers and the process of invention*, Smithsonian Institution, 1997.

[84] MOORE, A., and HARNEY, C., "Development of an integrated set of research facilities for the support of research flight test," *4th Flight Test Conference*, 1988, p. 2096.

[85] Corda, S., *Introduction to aerospace engineering with a flight test perspective*, John Wiley & Sons, 2017.

[86] Liu, T., and Schulte, M., "Flight Testing Education at Western Michigan University," *45th AIAA Aerospace Sciences Meeting and Exhibit*, 2007, p. 700.

[87] Liu, T., Mandziuk, M., Yurk, S., and Grashik, M., "Flight testing on Cirrus aircraft," *47th AIAA aerospace sciences meeting including the new horizons forum and aerospace exposition*, 2009, p. 571.

[88] Dantsker, O. D., Yu, S., Vahora, M., and Caccamo, M., "Flight testing automation to parameterize unmanned aircraft dynamics," *AIAA Aviation 2019 Forum*, 2019, p. 3230.

[89] Kimberlin, R. D., "Flight testing of fixed-wing aircraft, AIAA Educational Series," , 2003.

[90] Motter, M., Logan, M., French, M., and Guerreiro, N., "Simulation to flight test for a UAV controls testbed," *25th AIAA Aerodynamic Measurement Technology and Ground Testing Conference*, 2006, p. 3305.

[91] Jordan, T., Foster, J., Bailey, R., and Belcastro, C., "AirSTAR: A UAV platform for flight dynamics and control system testing," *25th AIAA Aerodynamic Measurement Technology and Ground Testing Conference*, 2006, p. 3307.